Sara N. Tourscher

Elemental Geochemistry, Mineralogy and Mass Transfer in Fault Segments of the San Andreas Fault Observatory at Depth (SAFOD) Drill Hole

Submitted for publication in: Geophysical Research Letters

in lieu of thesis in partial fulfillment
of the requirements for the degree of
Master of Science in Geology
Department of Geological Sciences
The University of Michigan

Accepted by:

Signature	Ben van der Pluijm	04/03/07
	Name	Date
Signature	Joel D Blum	04/09/07
	Name	Date
Department Chair	Rodney C. Ewing	04/11/07
	Name	Date

I hereby grant the University of Michigan, its heirs and assigns, the non-exclusive right to reproduce and distribute single copies of my thesis, in whole or in part, in any format. I represent and warrant to the University of Michigan that the thesis is an original work, does not infringe or violate any rights of others, and that I make these grants as the sole owner of the rights to my thesis. I understand that I will not receive royalties for any reproduction of this thesis.

☑ Permission granted.
☐ Permission granted to copy after: _____ Date
☐ Permission declined.

Sara Tourscher
Author Signature

Contents

Contained in this thesis is a paper- "Elemental Geochemistry, Mineralogy and Mass Transfer in Fault Segments of the San Andreas Fault Observatory at Depth (SAFOD) Drill Hole" that will be submitted to Geophysical Research Letters. This paper describes our study of plucked fault grains from two segments of the San Andreas Fault. All of the samples in this study were collected from SAFOD. I appreciate all the hard work people put into collecting the samples and the opportunity I was given to work on these samples. I compared the geochemistry of the plucked fault rocks to bulk rock and plucked host rocks. Recognizable differences were seen and mass transport was calculated using the isocon method. X-Ray diffraction analysis was used to determine mineralogy of several plucked fault rock samples.

There are 8 figures included in the first paper. Figure 1 is a location map of California; 2 shows a schematic of the drill hole including lithologies and the fault segments of interest; 3 shows the XRD analysis from 3075 m measured depth (MD), 3170 m MD and from 3344 m MD; 4 gives two back-scatter SEM images (from 3066 m MD and from 3436 m MD; 5 gives the elemental concentrations (in weight % oxide) of the plucked fault rocks; 6 shows isocon diagrams from four depth ranges (3069-3158 m MD, 3160-3170 m MD, 3292-3316 m MD, 3320-3368 m MD); 7 shows major element comparisons from the shallow trace of the fault; 8 shows major element comparisons from the main trace of the fault. There are two table included in the text. Table 1 gives concentrations of plucked fault rock and bulk rock for the shallow and deep sections of the shallow and main traces of the fault. Calculated mass transport is also given. Table 2 gives the calculated mass change for each oxide in each of the four sections studied.

Appendix A contains more detailed methods and procedures for the work done on the SAFOD samples. Appendix B includes all of the geochemical data used for the paper including plucked fault rock, bulk rock and plucked host rock samples; these data are plotted in Figures 5-8. Appendix C contains "The age of exhumed friction melts along the Alpine Fault, New Zealand" by Laurence Warr, Ben van der Pluijm and me. My contribution to this work included geochemical analysis of the pseudotachylytes and also some SEM work. This paper is in press, Geology 2007.

I would like to thank my advisor, Ben van der Pluijm, for his support and guidance through these two projects. Also, Anja Schleicher and Laurence Warr have been very helpful and their insights are invaluable. John Solum has been a big help to me through my time at Michigan and I am especially thankful for his help collecting samples in California. My fellow PASTEL group mates, Sam Haines, Belen Oliva, Jim Hnat, Alexandra Abrajevitch, Josep Pares and Rob van der Voo have been great and I appreciate their words of wisdom along the way. Without access to RIGL, this project may not have been possible; thank you Joel Blum, Marcus Johnson and Carmen Nezat for your assistance. Tom Eiting and Kelsey Johnson have been great inspirations to me and have helped me stay motivated. Finally, I would like to thank my parents and my two brothers, David and Lee, for encouraging me as I went along and always supporting me.

Elemental Geochemistry, Mineralogy and Mass Transfer in Fault Segments of the San Andreas Fault Observatory at Depth (SAFOD) Drill Hole

Sara Tourscher, Anja Schleicher, Ben van der Pluijm and Laurence Warr

ABSTRACT

Detailed elemental geochemistry and mineralogy analysis of samples from Phase 2 drilling of the San Andreas Fault Observatory at Depth (SAFOD) is presented from a shallow trace (3066 m- 3169 m measured depths MD) and a main trace (3292 m-3368 m MD) of the fault. Bulk rock material and hand picked fault grains (approximately 1 mm in size), characterized by polished thin film surfaces and slickenfibers, were investigated by X-ray diffraction (XRD), scanning electron microscopy (SEM) and elemental geochemistry analysis.

Based on oxide data, systematic differences in elemental concentrations are observed between the bulk rock and plucked fault rock. Isocon diagrams show that most of the elements are depleted in the plucked fault rock compared to the bulk rock. In particular silica, calcium and sodium are lost and to a lesser extend potassium, iron and magnesium. Minimum mass loss between the bulk rock and plucked fault rock ranges from 17-58% in the four sections of the drill hole examined, with the greatest mass transport calculated in the shallow trace of the fault. Because the lowest percentage of fault rock in the bulk rock samples is also found in this section, ~60% is a likely minimum estimate for mass transport in the fault zone. The large amount of mass transfer within these fault traces and temperatures less than 115° C at ~ 3 km depths require extensive circulation of hydrous fluids for progressive dissolution and leaching of wall rock during faulting. Based on the amount of silica loss in plucked fault rock, fluid-rock

ratios on the order of 100 were calculated (ranging from 47-141). Whereas dissolution may be partly induced by disequilibrium between fluid and rock, stress-induced dissolution at grain contacts would be the main mechanism for widespread mineral transformation in these fault rocks based on localization of neomineralization at grain and fracture surfaces.

INTRODUCTION

The San Andreas Fault Observatory at Depth (SAFOD) in Parkfield, California (Figure 1) provides a natural laboratory to study the chemical and physical processes associated with active deformation, creep and earthquake generation (Hickman et al., 2004). The San Andreas Fault transitions from creeping to seismic behavior near Parkfield, California. In 2002, a vertical Pilot hole was drilled to 2.2 km depth into Salinian granite/granodiorite after drilling through pebbly sandstone. The main SAFOD hole, drilled during 2004 and 2005, is situated 1.8 km southwest of the surface trace of the San Andreas Fault and is vertical to a depth of approximately 1.7 km, where it begins a sub- horizontal descent in order to intersect the trace of the San Andreas Fault at around 2.7 km true vertical depth (Figure 2a). Phase 1 completed in 2004, drilled through Tertiary and Quaternary sediments, granite/granodiorite and into arkosic sediments (Draper et al., 2005, Hickman et al., 2005). Phase 2 activity occurred in the summer of 2005 and completed drilling to 3992 meters measured depth (MD) along the drill hole. This drilling extended into interbedded mudstone, siltstone and shale lithologies at the bottom of the hole (Draper et al., 2005, Hickman et al., 2005).

SAFOD sampling provides the opportunity to examine the relationship between clay formation and fluid- rock interactions in fault zones at depth. This significantly improves on studies of formation of fault-related gouge and fluid-rock interaction from exhumed rocks, which are often complicated by the occurrence of alteration and (near-) surface weathering.

Fault Rock Clays

Clays are common alteration products in shallow crustal faults <10 km (e.g., Wu et al., 1975), which may offer preferred migration paths for fluids (Townend and Zoback, 2000). Gouge, common in fault rock, can be formed by the mechanical breakdown of rocks to form cataclasite (Sibson, 1977; Chester and Chester, 1998), but also through fluid-assisted mineral reactions (Sibson, 1994; Evans and Chester, 1995; Vrolijk and van der Pluijm, 1999). Dissolution and precipitation reactions, for example the breakdown of feldspar to clay, are commonly observed (e.g., Janecke and Evans, 1988). Indeed, clay gouge has been previously recognized in the San Andreas Fault System (e.g., Wu et al., 1975, Solum et al., 2003) with the potential to greatly influence the energetics of earthquake rupture (Wilson et al., 2005).

Clay growth occurs by fluid-assisted chemical alteration of unstable minerals in aqueous fluids, typically preexisting clays of feldspar phases. There are several hypotheses for the source of fluids and elevated fluid pressures within the San Andreas Fault system, including metamorphic fluids (Irwin and Barnes 1975), mantle devolatization (e.g., Kennedy et al., 1997 and Rice, 1992), tectonic compaction of sediments (Berry, 1973) and fault zone creep compaction (e.g., Sleep and Blanpied,

1992). The fluid chemistry from the SAFOD drill hole at 3065 m is described as a Na-Ca-Cl type fluid, which is typical of formation waters from sedimentary rocks in California (Thordsen et al., 2005). $^{3}He/^{4}He$ ratios for gasses dissolved in SAFOD drill hole fluids also indicate a mainly crustal origin (Thordsen et al., 2005).

Despite recognizing the presence of clays in fault zones, the precise role of clay formation in these zones and associated fluid-fault interaction are not sufficiently understood (Chester and Logan, 1986; Evans and Chester, 1995; Vrolijk and van der Pluijm, 1999). The goals of this study are to describe the SAFOD mineralogy and especially to quantify elemental differences between bulk rock and fault rock samples in order to understand the roles of neomineralization and mass transport in today's San Andreas Fault Zone. We emphasize that prior observations (Schleicher et al., 2006) showed that growth of clay occurs at microscopic scales, so it is critical to study fault rock geochemistry at the grain scale. Both bulk mineral assemblages and elemental composition of the San Andreas Fault rocks have been previously reported, (e.g. Evans and Chester, 1995; Chester and Chester, 1998; Solum et al., 2006), but elemental changes associated with discrete, thin fault surfaces at depth have not been considered. This paper focuses on individually picked fault grains from various depths in sections from the SAFOD drill hole and compares them with the adjacent bulk rock lithologies. Data collected in this study will demonstrate the extent of mineralization and mass transport and describe fluid-rock interactions and alteration in the modern San Andreas Fault.

Two areas of primary interest are targeted in this study: a shallow (ancient?) trace of the fault, around 3066 m based on gouge recovered from that depth, and samples around 3322 m, which is the active trace of faulting based on casing deformation seen from

3300-3353m (Zoback et al., 2005; Solum et al., 2006). The elemental geochemistry of 10 major and 3 minor elements for 36 plucked fault rock samples, for 27 plucked host rock samples and for 21 crushed bulk rock samples, ranging in depths from 3060 m to 3368 m, were analyzed. Backscattered SEM observations and XRD analysis show which minerals are altered and which have grown.

METHODS

Rock cuttings from Phase 2 drilling were collected from the shale shaker at 3 meter intervals. The cuttings were washed on 140 mesh screen (0.106 mm mean opening size) using fresh water. Air dried samples were sent to the United State Geological Survey (USGS) in Menlo Park, CA, from which split samples were collected for use in this study. All of the cuttings are labeled in feet measured depth (MD) along the borehole and converted to meters MD for this paper.

Two sections of the San Andreas Fault drill hole were selected for systematic analysis; a shallow fault trace (3069 m to 3078 m and 3139 m to 3179 m) and the main fault trace (3292 m to 3368 m). Fault grains were separated from the bulk rock samples, which avoided potential contamination from walnuts shells and steel shavings associated with drilling within each sample. In contrast to prior approaches (e.g., Solum et al., 2005) using bulk-rock material, plucking the fault grains from each sample is required for accurate characterization of the fault rocks, because it recognizes small-scale heterogeneities that are associated with fault surfaces. Samples in 3 meter intervals were chosen from section 1- the shallow trace from 3069 m to 3078 m and 3139 m to 3179 m, and section 2- the main trace from 3292 m to 3368 m. A magnet was used to attract

magnetic material (mostly steel shavings associated with drilling) from each sample. Once the magnetic material was removed, the remaining cuttings were examined under a microscope with the purpose of identifying and plucking of fault grains. The extremely fragile, dark gray fault grains, mainly less than 1 mm in size, were identified and hand-picked by the presence of polished surfaces and thin films with slickensides. Host rock grains (1-5 mm in size), which were mainly feldspar and quartz, were also plucked from the samples based on their lack of any polished surface.

Many of the grains in both host rock and fault rock samples had a rust colored coating. The samples were therefore rinsed for ~ 1 minute in deionized water in an ultrasonic bath. Once the samples were dried they were re-examined under the microscope to ensure that the coating had been removed. The samples were then weighed to ensure there was enough material for analysis. Finally, samples were powdered using a mortal and pestle.

The mineral assemblage of selected bulk rock, plucked fault grains and host rock samples were determined using a Scintag X-Ray Diffractometer at the University of Michigan Electron Microbeam Analysis Lab (EMAL). Random powders, oriented air-dried texture, and glycolated samples were prepared to characterize the bulk and clay mineralogy. Preparation of rocks followed the analytical methods described by Moore and Reynolds (1997). The samples were treated with ethanol glycol which causes interlayer expansion (shift of reflections toward higher d-values) and thus allows recognition of discrete smectite and mixed layered illite-smectite phases. As pure illite is not a swelling clay it is not affected by this treatment. The samples were analyzed using CuKα radiation, measurements varied from 2-70 °2θ with a step size of 0.02°2θ.

Complementary Scanning Electron Microscopy (Hitachi S3200N SEM) and semi-quantitative Electron Dispersive Spectroscopy (EDX), also housed in U-M's EMAL, were used to determine the mineralogy and mineral relationships from above section 1 at 3066m and from approximately 200 m below section 2 at 3436 m measured depth. These samples were chosen because of their proximity to the areas of interest.

Elemental geochemistry of bulk rock, plucked fault rock and plucked host rock samples was obtained at the University of Michigan's Radiogenic Isotope Geochemistry Laboratory and at the Keck Laboratory. Major (Al, Si, Ba, Ca, Fe, K, Mg, Mn, Na, P) and minor elements (Rb, Ti and Zr) were analyzed using an Inductively Coupled Plasma-Optical Emission Spectrometry (ICP-OES) and Inductively Coupled Plasma-Mass Spectrometry (ICP-MS). Comparison between ICP-OES and ICP-MS for several samples showed errors of 10% or less for most elements. ICP-OES was chosen as the preferred tool for elemental analysis, because of the number of samples that could be analyzed and the relative ease of the analytical procedure, while offering sufficient data quality. Powdered rock samples (100 mg) were digested in 5% Trace Metal HNO_3 with 1 g of ultra pure fused anhydrous lithium metaborate and 100 mg of lithium bromide (a non-wetting agent included to facilitate melting). Mn solution was used to align the view of the ICP-OES. The ICP-OES was calibrated using a blank and 6 dilutions (1/10, 1/50, 1/100, 1/500, 1/1000, and 1/5000) of SM-225102 -a certified digest standard (ordered from High Purity Standards). Quality control samples, River-sediment B, Trace Metal Drinking Water and SM-90 were chosen as they include all of the elements analyzed for; they were measured after every ten samples to check for instrument drift. All of the calibration and quality control standards were purchased from High Purity Standards,

except for SM-90, which was purchased from VHG Labs. USGS standards QLO-1, RGM-1, SCo-1, BHVO-1 and SDC-1 (Abbey, 1983; Gladney and Roelandts, 1988; Govindaraju, 1994; Flanagan, 1976) were also analyzed and used to routinely correct the measurements.

Results were converted to weight percent oxides (wt %) and used to calculate mass transport with the isocon method (Grant, 1986), which is a modification of Gresens' (1967) composition-volume diagrams. The isocon method calculates the slope of a line of equal concentration between altered rocks and their less-altered or unaltered counterparts. The concentration of the protolith is plotted along the x-axis and the concentration of the altered rock is plotted along the y-axis. In our study, the slope of the line is the ratio of the concentration of immobile elements (TiO_2 and ZrO_2) in the plucked fault rock to the concentration of that immobile element in the bulk rock. In general, Ti and Zr are used as immobile elements in isocon calculations (Grant, 1986; O'Hara, 1988; Cartwright and Barnicoat, 2003; Streit and Cox, 1998; Whitebread and Moore, 2004). To plot the isocon, the average of the TiO_2 and ZrO_2 slopes was used, which are typically within error for all but the shallowest section of main trace, where it was very close to fitting both TiO_2 and ZrO_2, using error bars of 1 standard deviation. Elements that plot above the isocon line would be enriched in the fault rock and elements that plot below the line would be depleted in the fault rock. If the slope is greater than 1, overall mass loss in the fault rock is indicated; if the slope is less than 1, overall mass gain in the fault rock occurred (e.g., Whitbread and Moore, 2004). The inverse of the slope, that is the composition of the bulk rock immobile elements divided by the plucked fault rock immobile elements, is used to calculate the bulk mass transport and the mass transport for each element. An example

calculation for the total mass transport using TiO_2 as the immobile element is show in equation 1 based on Grant's method (1986). We similarly use C_i to denote concentration of an element i, while the superscripts O and A represent original and altered, respectively. Equation (1) gives the percent change of an element.

$$\Delta C_i/C_i = (C^O_{TiO2}/ C^A_{TiO2})* (C^A_i/C^O_i)-1 \quad (1)$$

The change in individual element concentrations is determined based on their distance from the isocon (Olsen and Grant, 1991); calculated by Equation (2).

$$\Delta C_i = (\Delta C_i/C_i)* C^O_i \quad (2)$$

Appendix A contains more details about the methods used in this study.

RESULTS

Mineralogy

X- Ray Diffraction Analysis

The XRD analyses from the randomly oriented bulk rock samples show quartz, feldspar (plagioclase and K-feldspar) and clay minerals (illite, illite-smectite) as main mineral assemblages, with additionally chlorite and/or chlorite-smectite in the deeper areas (see also Solum et al., 2006). The plucked fault rock material contains primarily illite and illite-smectite minerals with minor quartz and plagioclase components and as well chlorite and/or chlorite-smectite in the deeper areas.

Variations in the illite and illite-smectite occurrence were observed by comparing XRD patterns of oriented samples from the bulk rock and the plucked fault rock. Based on the illite and illite-smectite peak position and peak shape, the plucked fault rock samples contain the most illitic and smectitic components compared to the bulk rock

material. Variations in amount and ordering of illite and illite-smectite phases are also recognizable within the fault rocks at different depths. The X-ray diffraction patterns of air-dried and glycolated, oriented samples for three plucked fault rock samples - two from the shallow trace of the fault and one from the main trace of the fault are presented in Figures 3A-C.

Shallow Trace

Representative samples between 3075 m and 3170 m MD were analyzed by XRD. The diffraction pattern of the plucked fault grains at 3075 m MD (Fig. 3A) shows a broad peak in the air dried sample with two maxima. This broad peak is caused by the combined contribution of two phases; one at ca. 10.0 Å representing a pure illite phase, and one at ca. 11.0 Å indicating an illite-smectite phase. After glycolization, the smectitic component shifts the peak towards higher d-values at ca 12.0 Å, whereas the non-swelling illite phase remains at 10.0 Å (Figure 3A). The glycolization causes an expansion of the smectite phase and reduces the influence of the smectite layers on the illite reflection, thus provoking a shift to lower d-values. This is characteristic of relatively small amounts of interlayer smectite and a high degree of ordering (Moore & Reynolds, 1997). The diffraction pattern of the fault grains from the deepest sample in the shallow area (3170 m MD, Fig. 3B) also shows typical illite and illite-smectite components in form of a broad peak with two maxima. Here, the illite-smectite peak occurs at 10.6 Å, reflecting less smectite interlayers. The chlorite peak at 14.5 Å probably overlaps the smectitic peak at higher d-values after glycolization. The illite peak remains again at 10.0 Å. The occurrence of chlorite at 3170m MD reflects a lithological change around 3158 m MD (Draper et al., 2005).

Main Trace

X-ray analysis from fault rocks of the main trace section show the same components of illite and illite-smectite (Fig. 3C). However, based on the peak shape and the peak position of illite and smectite, an illite-smectite mixed layering with a higher amount of smectitic layers occurs in most of the samples. The sample at 3344 m MD for example, show a typical illite peak at 10.0 Å in the air dried state. A shift in the illite peak is not seen when glycolated, but the shapes of the air-dried and glycolated curves create a broad peak between 11 and 12 Å, which indicates the presence of a more smectite rich illite-smectite phase than in the shallow fault. A small shift of the chlorite peak in the glycolated samples indicate a chlorite-smectite phase that could be observed in most of the XRD patterns observed at this depths.

SEM Observations

To illustrate mineralogy and microstructures of the samples analyzed and compare direct observations with the mineral assemblages determined by X-ray diffraction, Figure 4 shows representative backscattered electron images from a) 3066 m MD (3 m above the shallow trace) and b) 3436 m MD (68 m below the main trace). The SEM images confirm the mineral assemblages detected by XRD in the analyzed traces, with quartz, feldspar, chlorite and clay minerals as main components. Based on the strongly altered rims of these minerals, dissolution/precipitation reactions reveal the main process producing clay minerals in all samples investigated. Fig. 4A shows plagioclase minerals (mostly a mixture of albite and anorthite) in the shallow sample at 3066 m MD that are altered into illite and illite-smectitic clay minerals. The EDX patterns of these

illite minerals show a relatively high amount of potassium and mostly no sodium in the interlayer sheets, next to magnesium and less iron in the octahedral sheets. Illite that nucleates in small pores based on dissolution/precipitation reactions shows mainly potassium, sodium and less calcium in the interlayer sheets, next to magnesium and iron in the octahedral layers, indicating a smectitic component. The deeper samples at 3436 m MD (Fig. 4B) also contain strongly altered minerals with diluted rims and irregular fractures that are partly filled with illite and illite-smectite minerals. These veins are in general 10-20 micron in thickness, whereas the illite fillings show a slightly preferred orientation along the veins. These textures demonstrate nucleation and growth of clays along the irregular fractures. Feldspar dissolution as well as chloritization of biotite is optically recognized, in support of the elemental changes described below.

Geochemistry

The elemental concentrations of all plucked fault samples are plotted in Figure 5, showing the shallow trace (3060 m – 3170 m MD) and the deep main trace (3290 m – 3370 m MD) of the cored SAF. A general decreasing element distribution with depth can be recognized in most of the elements, except of Si and Al that remain relatively stable. Because of an elemental shift based on a lithological change at 3158 m MD (Draper et al., 2005) the shallow trace of the fault is divided into two sections. Whereas the Zr, Mn, Ti, Na and K element concentrations decrease, Si, Al, Ca, Mg, and Fe do not show a notable change. Another change in element concentration can be recognized between 3315 m and 3320 m MD, which divides the main trace into two groups- the shallow section from 3292 m to 3316m MD and the deeper section from 3319m to 3368 m MD (dashed line).

At these depths, casing deformation shows the activity in this region (Zoback, et al., 2005). The elements Zr, K and Si remain relatively stable, whereas Mn, Ti, Na, Mg, Fe and Al show an increase in concentration. Ca shows no clear trend in the main fault that may reflect a change in smectitic interlayers in the fault rocks. Appendix B tabulates oxide data for these samples.

Isocon Analysis

Isocon diagrams (Grant, 1986), which are created by plotting the composition of an altered rock against its less or unaltered counterpart, are used to calculate mass transport. For this study, the average composition of plucked fault grains is plotted against an average bulk rock sample. While plucking fault grains is a significant improvement over bulk analysis of fault rock used in prior studies, it is important to emphasize that this approach still offers lower estimates of transport, because the bulk rock samples will include fault material in varying amounts. Host rocks were also plucked from bulk rock samples, but a calculation based on comparing plucked fault rocks to plucked host rocks is likely biased, because the only unequivocal type of host rocks are quartz and feldspar grains. Figure 6 shows the isocon diagrams with the isocon based on the immobile elements Ti and Zr, and the 1:1 isocon for the four sections of the fault examined.

Shallow Trace

The shallowest segment of fault rock that was studied (3069 m to 3158 m MD) preserves the greatest amount of mass transport among the four areas in this study. As seen in Figure 6A the slope of the isocon is 2.4, indicating a mass loss of up to 58%

between the bulk rock and the fault rock. TiO_2 and ZrO_2 (immobile oxides) both fall on the isocon, while Rb_2O, MnO and MgO fall close to the isocon within error, indicating that they are also mostly immobile in this system. P_2O_5 is slightly enriched in the fault rock, but not significantly at the error level. SiO_2, Al_2O_3, Na_2O, CaO, K_2O, Fe_2O_3 and BaO are mobile phases in the system and represent the main elements depleted during alteration and fault rock formation.

The deeper part of the shallow trace, at 3160 m- 3170 m MD, where the mudstone/ shale/ siltstone units appear, shows less mass transport (Figure 6B). The isocon slope is 1.4, equating to a mass loss of 29%. As before, TiO_2 and ZrO_2 fall along the isocon, while Rb_2O, MnO, P_2O_5 and MgO fall close to the isocon indicating their immobility. Al_2O_3, K_2O, and Fe_2O_3 similarly lie away from the isocon, but less than in the shallower section. Table 1 summarizes the total calculated mass transport, mass transport per oxide and the average compositions for the fault rock and bulk rock that were used in the calculation. The percent change for each element is listed in Table 2.

Main Fault Trace

The main trace of today's San Andreas Fault is separated into two sections (shallow- 3292m to 3316 m MD, and deep- 3319m to 3368 m MD), based on compositional differences shown in Figures 2b and 5. The isocon for the shallower section, as before based on TiO_2 and ZrO_2, has a slope of 1.6, indicating a minimum mass loss of ~38% between bulk rock and fault rock. As seen in Figure 6C, Rb_2O and P_2O_5 lie on the isocon within error. Mobile elements include SiO_2, Al_2O_3, Na_2O, CaO, K_2O, Fe_2O_3, MgO, MnO and BaO.

The isocon for the deeper section has a slope of 1.2 representing a total mass loss of 17% between bulk and fault rock (Figure 6D). Most of the elements plot close to the isocon, with CaO and BaO appearing to be the most mobile elements in the system. The calculated mass change per element and the total calculated mass transport for both sections of the main trace are given in Table 1; Table 2 lists the percent change for each element.

Major Element Comparisons

The isocon method allows for the calculation of mass changes between the fault rock and its less altered counterpart; however, in order to understand the relative behavior of elements, major elements comparisons are needed.

Shallow Trace

Figure 7 shows the major elements Al, Ca, Fe, K, Mg and Na plotted against SiO_2 from the shallow trace. Also, ZrO_2 is compared to TiO_2 because they were both used as immobile elements. Each plot shows plucked fault rock (diamonds), plucked host rock (squares), and bulk rock concentrations (circles). Based on lithologic changes discussed earlier in the paper, the plucked fault rock concentrations are broken up into two groups. The element concentration of the lower part of the shallow fault zone is similar to the bulk rock concentrations, whereas the upper part shows stronger differences in weight %. In general, the fault rock elemental concentration of Al, Fe, and Mg is higher than the bulk rock concentration, higher and/or similar in K and lower in Ca and Na. The decreased amount of Ca and Na in the fault rock samples may be due to the alteration of plagioclase (albite and anorthite) in the system and the occurrence of varying amount of

illite, illite-smectite mixed layers in the rocks. We note that the high amount of Mg and Fe in the fault rocks could be a result of chlorite in the fault rocks. See Appendix B for the data tables.

Main Trace

Major element comparisons to SiO_2 for the main trace are shown in Figure 8. Clearly different trends between the fault rock and the bulk rock can be recognized in the Al, Ca, Fe and Na concentrations, whereas K and Mg show similar trends and concentrations in both the fault rock and the bulk rock. Na and Ca are strongly depleted in the fault rocks, most likely due to the feldspar dissolution as previously mentioned.

DISCUSSION

This study offers a detailed analysis of elemental geochemistry of plucked fault rocks from the San Andreas Fault drill cuttings. Our approach highlights the importance of selecting fault material (via plucking) in order to obtain a reliable understanding of geochemical processes in heterogeneous shallow faults, as opposed to bulk analyses that assume homogenization.

Elemental Changes

The isocon method involves the concentration of bulk samples from faults and the unaltered or a less altered protolith. In this study, we use plucked fault rock and bulk rock. The bulk rock is not exactly unaltered protolith contains varying amounts of fault material, so all of the changes will be minimum estimates. Because there is much less fault material in the bulk rock samples from the shallow trace of the fault than in the bulk

rock samples from the main trace of the fault, the latter underestimates elemental changes most.

The relatively large mass loss calculated in this paper, as high as 50%, is a minimum estimate, because the bulk rock contains some fault rock and therefore underestimates change. The change of elemental composition shows that a large percent of many elements, mainly Ca, Si, Na and Ba, has been lost; this is seen in Table 2 and Figure 6. Ba is an additive used in drilling, so the loss of Ba suggests no contamination from drilling mud. The large loss of Ca, Na and Si is due to the dissolution of feldspars that is also observed in SEM images. Al, K, Mg and Fe show a smaller loss because they are incorporated into clays- for example interlayer K in illite and octahedral Fe and Mg in chlorite.

The relative enrichment of immobile oxides (TiO_2 and ZrO_2) is caused by volume losses of up to ~60%. The amount of calculated mass transport decreases with depth within each fault trace, which could be interpreted to mean that the reactions and amount of fluid transport in the shallowest section of each fault trace was greater than the amount of fluid circulated in deeper sections. However, the results more likely reflect the higher percentage of fault rock in the bulk rock sample of the main trace, which is corroborated by qualitative evidence from the bulk rock drill cuttings, showing that with depth the percentage of fault material in the bulk rock cutting samples increases.

Mass balance and volume- composition calculation

Modifying Gresens' (1967) volume – composition calculation the following mass balance equations can be written for each of the four sections of fault examined in this

paper. For the purpose of this study, the ratio of the density of bulk rock to plucked fault rock is assumed to be 1, reflecting that the types of rock are similar.

100g of bulk rock – 47.01g SiO_2 – 6.04g Al_2O_3 – 2.16g Na_2O – 1.30g K_2O – 1.13g CaO – 0.55g Fe_2O_3 – 0.23g BaO – 0.01g Rb_2O = 41.14 g fault rock + 0.30g MgO + 0.09g TiO_2 + 0.03g P_2O_5 + 0.01g MnO

(upper section of shallow trace, 3069-3158 m measured depth)

100g of bulk rock – 23.50g SiO_2 – 2.20g CaO – 1.65g Al_2O_3 – 0.61g Na_2O – 0.56g Fe_2O_3 –0.36g K_2O – 0.11g BaO – 0.03g MnO = 70.96g fault rock + 0.02g TiO_2 + 0.01g MgO

(lower section of shallow trace, 3161-3169 m measured depth)

100g of bulk rock – 31.53g SiO_2 – 3.07g CaO – 1.21g Fe_2O_3 – 0.66g Al2O3 – 0.61g Na_2O – 0.50g MgO – 0.34g K_2O – 0.07g BaO – 0.5gMnO = 61.96 g fault rock + 0.04g TiO_2

(upper section of main trace, 3292-3316 m measured depth)

100g of bulk rock – 16.17g SiO_2 –1.81g CaO – 0.26g Na_2O – 0.21 K_2O – 0.05 BaO – 0.02 MnO = 77.99 g fault rock + 0.80 g Al_2O_3 + 0.52 Fe_2O_3 + 0.09g MgO + 0.09 gTiO_2

(lower section of main trace, 3219-3368 m measured depth)

The greatest loss in all cases is that of SiO_2. In the shallower sections, CaO, Na_2O and K_2O are lost in all samples. Al_2O_3 is lost in all samples but the deepest sample. The

greatest preserved loss is in the shallowest sample and the least preserved loss is in the deepest sample. The deepest sample shows the least change because the bulk rock contains the most fault rock material; likewise, the shallowest sample contains the least fault material in the bulk rock.

Alteration Reactions

Based on elemental geochemistry, XRD patterns and SEM images the following mineral transformations have occurred in the San Andreas Fault at the depths discussed in this paper.

$3NaAlSi_3O_8 + K^+ + 2H^+ \longrightarrow KAl_3Si_3O_{10}(OH)_2 + 6SiO_2 + 3\,Na$

Albite illite quartz

$3CaAl_2Si_2O_8 + 2K^+ + 4H^+ \longrightarrow 2KAl_3Si_3O_{10}(OH)_2$

Anorthite illite

$KAlSi_3O_8 + 2/3H^+ \longrightarrow 1/3\ KAl_3Si_3O_{10}(OH)_2 + 2SiO_2 + 2/3K^+$

K-feldspar illite quartz

Biotite $\longrightarrow$ chlorite + titanite + H_4SiO_4 + Fe + Al + Na + K^+

(Veblen, 1992)

Illite, illite-smectite, smectite, chlorite and chlorite-smectite are the main alteration products seen in the samples studied. Illite is formed by dissolution of feldspars and smectite from the alteration of illite. K-feldspar is rare in the 3066m and 3434m samples compared to plagioclase and quartz, according to back-scatter SEM images. XRD analysis of bulk rock and plucked fault show a decrease in K-feldspar in the plucked fault rock indicating that much of the feldspar has been altered to illite during faulting.

Implications for Fluid: Rock Interaction

A system open to fluids is necessary to allow the depletion of the elements in each of the fault sections examined. Fluids are needed to dissolve and transport elements from the host rock and precipitate new phases in the fault zones. Grain coatings indicate that boundary fluids are responsible for neomineralization in these rocks. Grain coatings also indicate that any strength property is defined by grain-grain interfaces, rather than bulk rock properties.

Using the temperature measurements from the SAFOD drill hole (Williams et al., 2005) at the relevant depths, molal (moles/kg) silica solubility is calculated based on Rimstidt's (1997) equation. The temperatures used for these calculations were 110° C for the shallow trace and 114° C for the main trace. Converting the SiO_2 weight % oxide to moles of SiO_2 and using the molal solubility of silica fluid-rock ratios are calculated. These calculations give fluid: rock ratios that range from 47 to 141. In other cases of high mass transport, such high fluid ratios were common (e.g., O'Hara, 1988).

CONCLUSION

This study demonstrates the importance of studying plucked fault rocks in order to obtain an accurate representation of the highly localized changes within shallow fault zones. Because many of the alterations occur at grain boundaries, it is important to constrain any changes at these scales.

Based on oxide data, systematic differences in elemental concentrations are observed between bulk rock and plucked fault rock. Geochemical and XRD analysis of plucked grains is distinguishable from bulk rock analysis. Mass transport calculations,

ranging from 17% to 58% volume loss, show that almost all elements are depleted in the fault rock. In particular, Ca, Na and Si are lost and to a lesser degree Fe, Mg and K. Clay minerals bearing octahedral Fe and Mg (such as chlorite) and interlayer K (such as illite) and to a lesser extent Ca and Na (smectite) are formed from the chloritization of biotite and dissolution of feldspars. Elements that are associated with new minerals in cracks and neomineralized surfaces were lost less than those not incorporated into these clays, explaining the variation observed.

Extensive circulation of hydrous fluids is required for progressive dissolution and leaching of wall rock during faulting. Using the amount of silica lost, fluid: rock ratios, on the order of 100, were calculated. Dissolution is induced by disequilibrium between fluid and rock, but, based on the localized mineralization, stress-induced dissolution at grain-contacts may be the controlling mechanism for widespread mineral transformations in these fault rocks.

Acknowledgements

The National Science Foundation (EAR-0345985), the Deutsche Forschungsgemeinschaft (DFG Project SCHL 1821/1-2) and the University of Michigan Turner Fund provided support for our SAFOD research. Thanks to Joel Blum for providing generous access to RIGL and to Marcus Johnson and Carmen Nezat for their assistance in ICP-OES analysis and Ted Huston for ICP-MS analysis at the University of Michigan. Thanks to John Solum for helping to collect samples and many discussion on XRD analysis and SAFOD sampling.

REFERENCES

Abbey, S., (1983) Studies in "standard samples" of silicate rocks and minerals 1969-1982, Canadian *Geological Survey Paper 83-15*, p-114.

Berry, F.A.F., (1973) High fluid potentials in California Coast Ranges and their tectonic significance, *American Association of Petroleum Geologists Bulletin, 57*, 1219-1249.

Cartwright, I., and A.C. Barnicoat, (2003) Geochemical and stable isotope resetting in shear zones from Täschalp: constraints on fluid flow during exhumation in the Western Alps, *Journal of Metamorphic Geology, 21*, iss. 2, 143-161.

Chester F.M., and J.S. Chester (1998) Ultracataclasite structure and friction processes of the Punchbowl fault, San Andreas system, California, *Tectonophysics, 295*, 199-221.

Chester, F.M., and J.M. Logan, (1986) Implications for mechanical properties of brittle faults from observations of the Punchbowl Fault zone, California *Pure and Applied Geophysics, 124*, 79-106.

Draper, S.D., Boness, N.L., and J.P. Evans (2005) Source and significance of the sedimentary rocks in the SAFOD borehole: preliminary analysis, *Eos Trans. AGU, 86(52)* Fall Meet. Suppl., Abstract T24B-02.

Evans J.P., and F.M. Chester (1995) Fluid-rock interaction in faults of the San Andreas system; inferences from San Gabriel Fault rock geochemistry and microstructures, *Journal of Geophysical. Research, B, 100(7)*, 13,007-13,020.

Flanagan, F.J., (1976) Descriptions and Analyses of Eight New USGS Rock Standards, *U.S. Geological Survey Professional Paper 840*, p 192.

Gladney, E.S., and I. Roelandts, (1988) 1987 Compilation of Elemental Concentration Data for USGS BHVO-1, MAG-1, QLO-1, RGM-1, SCo-1, SDC-1, SGR-1, and STM-1, *Geostandards Newsletter, 12*, 253-362.

Govindaraju, K., (1994) 1994 Compilation of Working Values and Descriptions for 383 Geostandards, *Geostandards Newsletter, 18,* 1-158.

Grant, J.A., (1986) The isocon diagram- a simple solution to Gresens' Equation for Metasomatic Alteration, *Economic Geology, 81,* 1976-1982.

Gresens, R.L., (1967) Composition- volume relationships of metasomatism, *Chemical Geology, 2,* 47-65.

Hickman, S., Sibson, R., and R. Bruhn, (1995) Introduction to special section: Mechanical involvement of fluids in faulting, *Journal of Geophysical Research, 100,* 12831-12840.

Hickman, S.H., Zoback, M.D., and W.L. Ellsworth (2004) Introduction to special section: Preparing for the San Andreas Fault Observatory at Depth, *Geophysical Research Letters, 31*, L12S01- L12S04

Hickman, S.H., Zoback, M.D., and W.L. Ellsworth (2005) Structure and composition of the San Andreas Fault Zone at Parkfield: initial results from SAFOD Phase I and II, *Eos Trans. AGU, 86(52)* Fall Meet. Suppl., Abstract T23E-05.

Irwin W.P., and I. Barnes, (1975) Effect of geologic structure and metamorphic fluids on

seismic behavior of the San Andreas fault system in central and northern California, *Geology*, *3* no. 12, 713- 716.

Janecke, S.U., and J.P. Evans, (1988) Feldspar-influenced rock rheologies, *Geology, 16*, 1604-1607.

Kennedy, B.M., Kharaka, Y.K., Evans, W.C., Ellwood, A. De Paolo, D.J., Thordsen, J., Ambats, G., and R.H. Mariner, (1997) Mantle fluids in the San Andreas Fault System, California, *Science*, *278* 1278-1281.

Moore, D.M and R.C Reynolds, Jr., (1997) X-Ray Diffraction and the Identification of Clay Minerals. Second edition. Oxford University Press.

O'Hara, K., (1988) Fluid flow and volume loss during mylonitization: an origin for phyllonite in an overthrust setting, North Carolina, U.S.A., *Tectonophysics, 156*, 21-36.

Olsen, S.N., and J. A. Grant, (1991) Isocon analysis of migmatization in the Front Range, Colorado, USA, *Journal of Metamorphic Geology, 9,* 151-164.

Rice, J.R., (1992) in Fault Mechanics and Transport Properties in Rocks (eds. Evans, B. and Wong, T.F.) Academic, London 475-503.

Rimstidt, J. D., (1997) Quartz solubility at low temperatures, Geochimica et *Cosmochimica Acta, 61*, 2553-2558.

Schleicher, A.M, van der Pluijm, B.A., and L.N. Warr, (2006) Origin and significance of clay-coated fractures in mudrock fragments of the SAFOD borehole (Parkfield, California), *Geophysical Research Letters, 33*, L16313- L16317.

Schleicher, A.M, Warr, L.N., and B.A. van der Pluijm (2005) The clay mineralogy of

fracture coatings observed in mudrock cuttings from the SAFOD borehole, *Eos Trans. AGU, 86(52)* Fall Meet. Suppl., Abstract T21AB-455.

Sibson, R.H., (1977) Fault rocks and fault mechanisms, *Journal of the Geologic Society of London, 133*, 191-213.

Sibson, R.H., (1994) Crustal stress, faulting and fluid flow In : J. Parnell (ed.), Geofluids: Origin, Migration and Evolution of Fluids in Sedimentary Basins. *Geological Society Special Publication 78*, 69-84.

Sleep, N. H., and M. L. Blanpied (1992) Creep compaction and the weak rheology of major faults, *Nature, 359,* 687- 692.

Solum, J.G., B.A. van der Pluijm, (2004) Phyllosilicate mineral assemblages of the SAFOD Pilot Hole and comparisons with an exhumed segment of the San Andreas Fault System, Geophysical *Research Letters, 31,* L15S19- L15S22 phyllosilicate mineral assemblages, fabrics, and fluids on the behavior of the Punchbowl fault, southern California, *Journal of Geophysical Research, 108(B5).*

Solum, J.G., van der Pluijm, B.A., Peacor, D.R. and L.N. Warr, (2003) Influence of phyllosilicate mineral assemblages, fabrics, and fluids on the behavior of the Punchbowl fault, southern California, *Journal of Geophysical Research,* 108(B5).

Solum, J.G., Hickman, S.H., Lockner, D.A., and D.E. Moore, (2005) Mineralogy of the SAFOD Main Hole: Detailed Characterization of Fault and Country Rocks, *Eos Trans. AGU, 86(52)* Fall Meet. Suppl., Abstract T24B-01.

Solum, J.G., Hickman, S.H., Lockner, D.A., Moore D.E., van der Pluijm, B.A.,

Schleicher, A.M., and J.P. Evans, (2006) Mineralogical characterization of protolith and fault rocks from the SAFOD Main Hole, *Geophysical Research Letters, 33,* L21314- L21318.

Streit, J.E., and S.F. Cox, (1998) Fluid infiltration and volume change during mid-crustal mylonitization of Proterozoic granite, King Island, Tasmania, *Journal of Metamorphic Geology, 16*, 197-212.

Thordsen, J.J., Evans, W.C., Kharaka, Y.K., Kennedy, B.M., and M. van Soestim (2005) Chemical and isotopic composition of water and gases from the SAFOD wells: implications to the dynamics of the San Andreas Fault at Parkfield, CA, *Eos Trans. AGU, 86(52)* Fall Meet. Suppl., Abstract T23E-08.

Townend, J., and Zoback, M.D., (2000) How faulting keeps the crust strong, *Geology, 28 no. 5*, 399-420.

Veblen, D.R.. (1992) Electron microscopy applied to nonstoichiometry, polysomatism and replacement reactions in minerals, In: P.R. Buseck (ed.), Minerals and Reactions at Atomic Scale: Transmission Electron Microscopy. *Rev. Mineral. 27*, 181-223.

Vrolijk, P., and B.A. van der Pluijm, (1999) Clay gouge, *Journal of Structural Geology, 21*, 1039-1048.

Whitbread, M.A., and C.L. Moore, (2004) Two lithogeochemical approaches to the identification of alteration patterns at the Elura Zn-Pb-Ag deposit, Cobar, New South Wales, Australia: use of Pearce Element Ratio analysis and Isocon analysis, *Geochemistry: Exploration, Environment, Analysis, 4*, 129-141.

Williams, C.F., d'Alessio, M.A., Grubb, F.V., and S.P. Galanis, Jr., (2005) Heat Flow

Studies in the SAFOD Main Hole, *Eos Trans. AGU, 86(52)* Fall Meet. Suppl., Abstract T23E-07.

Wilson, B., Dewers, T., Reches, Z., and J.N. Brune, (2005) Particle size and energetics of gouge from earthquake rupture zones, *Nature, 434(7034),* 749-752

Wu, F.T., Blatter, L., and H. Roberson, (1975) Clay gouges in the San Andreas Fault system and their possible implications, *Pageoph, 133*, 87-95.

Zoback, M.D. and S.H. Hickman, (2005) Preliminary observations of stress and fluid pressure in and near the San Andreas Fault at depth in SAFOD boreholes, *Eos Trans. AGU, 86(52)* Fall Meet. Suppl., Abstract T21A-0438.

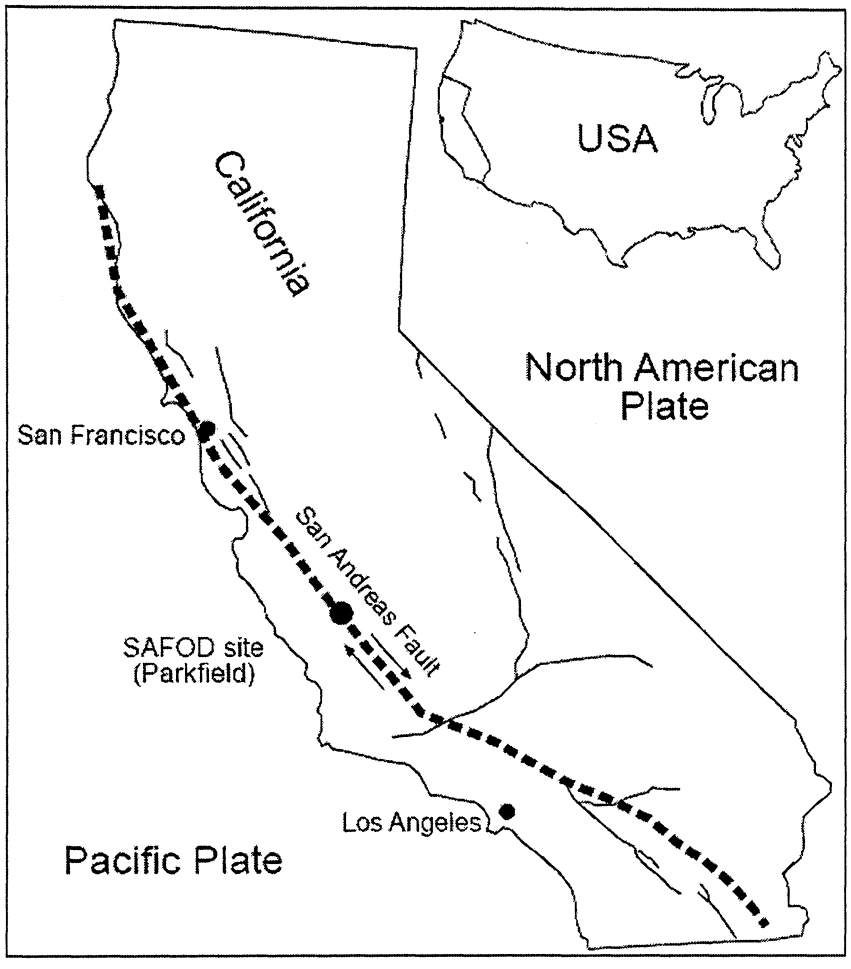

Figure 1: Map of USA and California with San Andreas Fault and the SAFOD site in Parkfield, California identified.

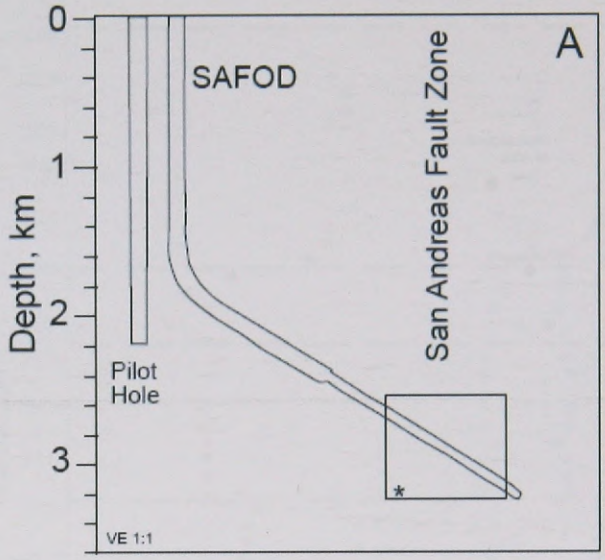

Figure 2: (A) Schematic of SAFOD (after Zoback, 2005 and Hickman, 2005). Box represents area of this study. Depth is shown on the vertical axis. VE is 1:1 (B) Zoom in of study area. Boundaries samples from the shallow creeping fault and main trace are shown. All measurements are in m measured dept. Modified after Draper, et al., 2005.

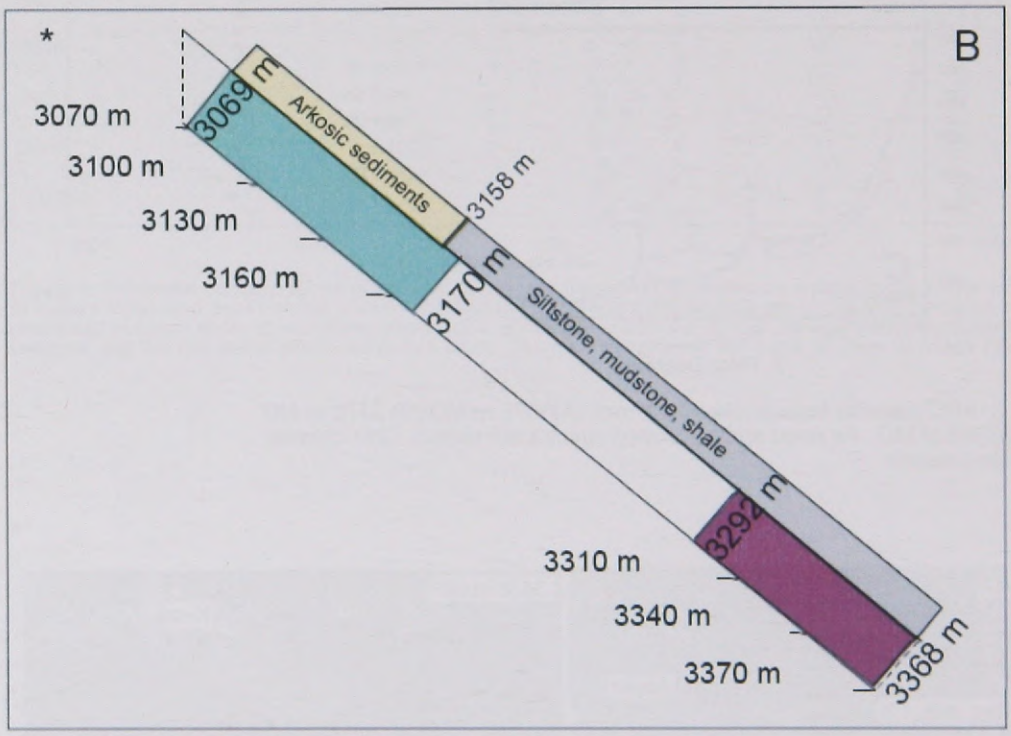

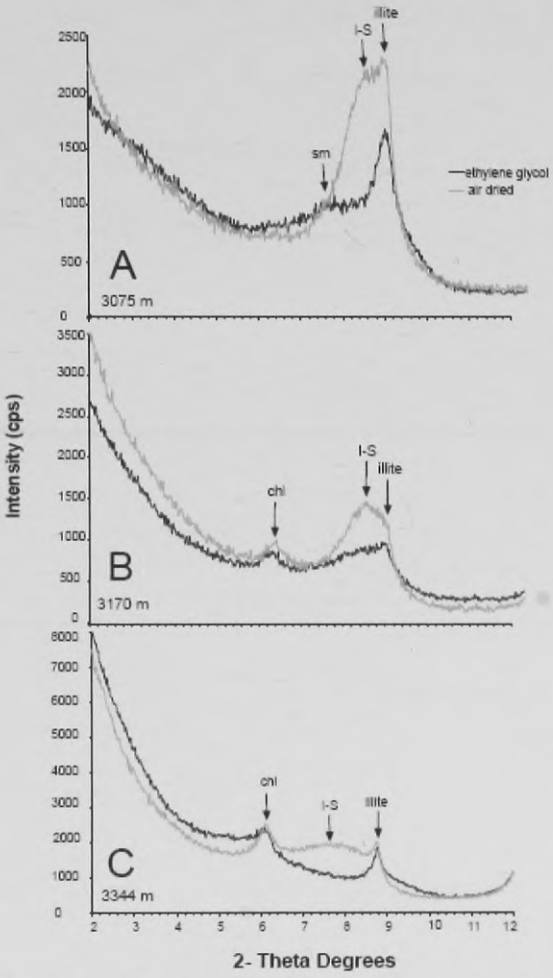

Figure 3: XRD patterns from plucked fault rock (A)3075 m MD (B) 3170 m MD and (C)3344 m MD. Air dried and glycolated spectra are shown. Chl= chlorite, I-S = illite-smectite.

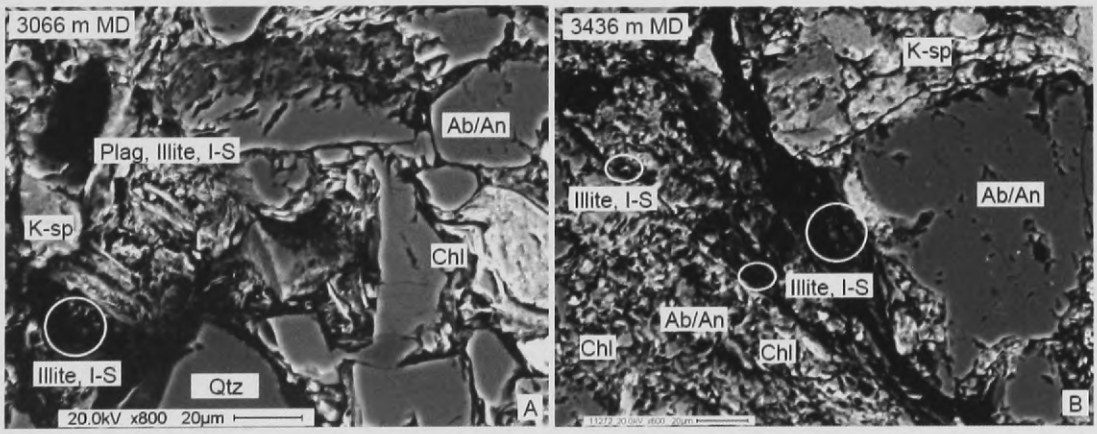

Figure 4: Back-scatter images from 3066 m measured depth (A) and 3436 m measured depth (B). Ab/An= albite/ anorthite, I/S= illite/ smectite, Chl= chlorite, Qtz= quartz, K-spar= potassium feldspar

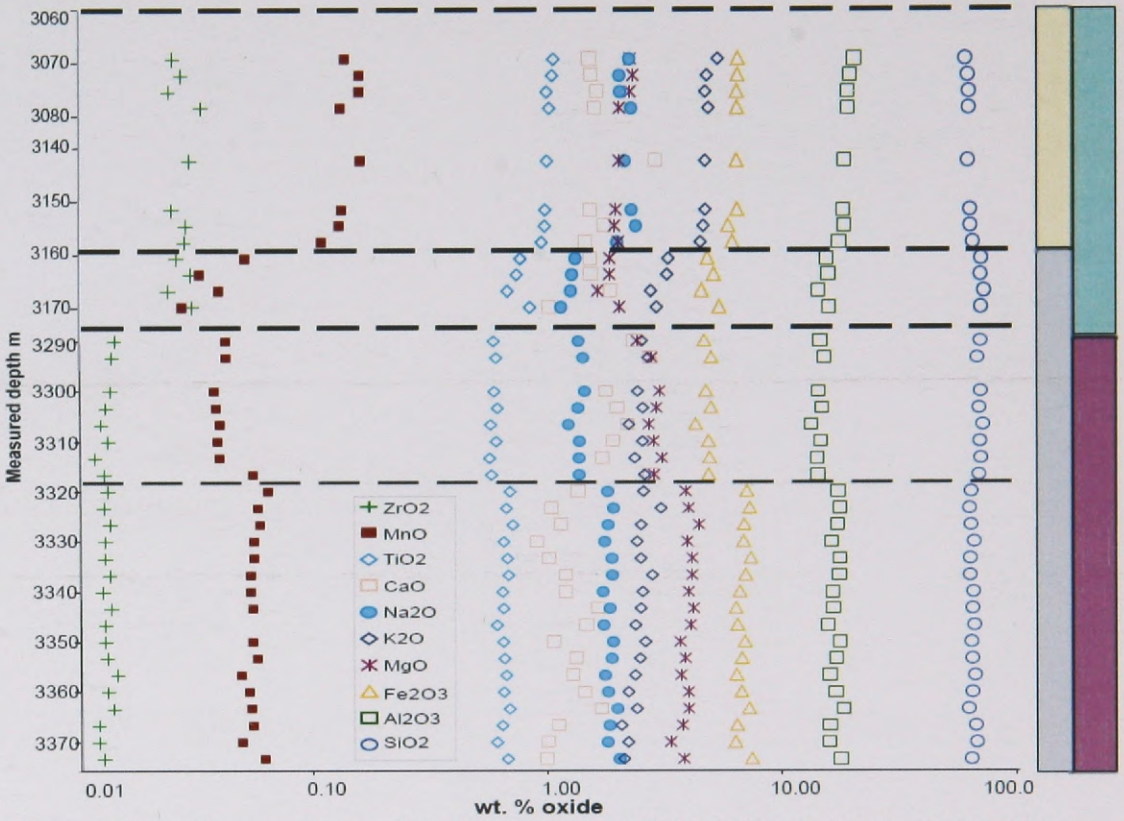

Figure 5: Elemental concentrations of plucked fault rocks from SAFOD plotted on a logarithmic x-axis with depth in meters measured depth on the y-axis. Dashed lines represent the boundaries of the fault sections. Oxides presented in key in order of increasing abundance. Colored bars on the right of the figure represent the lithology changes and the two faults examined in this study. The colors represent the same as they do in the Figure 2.

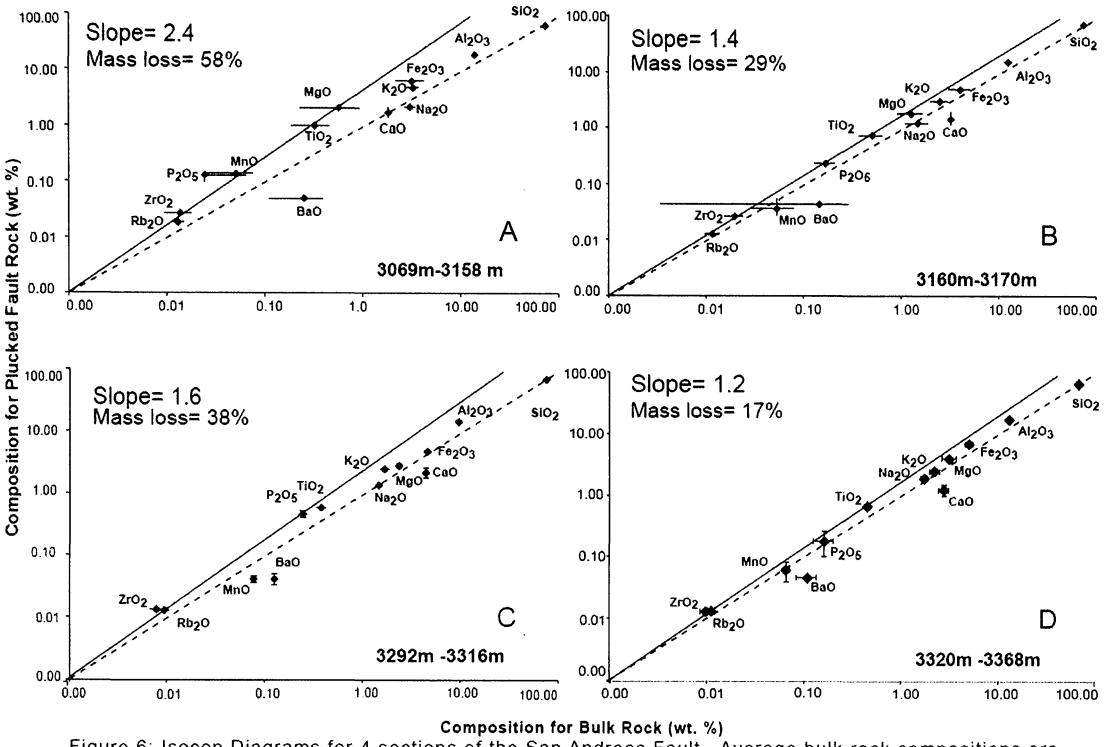

Figure 6: Isocon Diagrams for 4 sections of the San Andreas Fault. Average bulk rock compositions are plotted on the x- axis and average plucked whole rock compositions are plotted on the y-axis. Error bars are shown based on 1 standard deviation. The slopes of the isocons are calculated using TiO_2 and ZrO_2 as immobile elements. 1:1 slopes are shown as dashed lines. (A) Data from 3069-3158 m md (B) Data from 3160-3170 m md (C) Data from 3292- 3316m md (D) Data from 3320-3368m md.

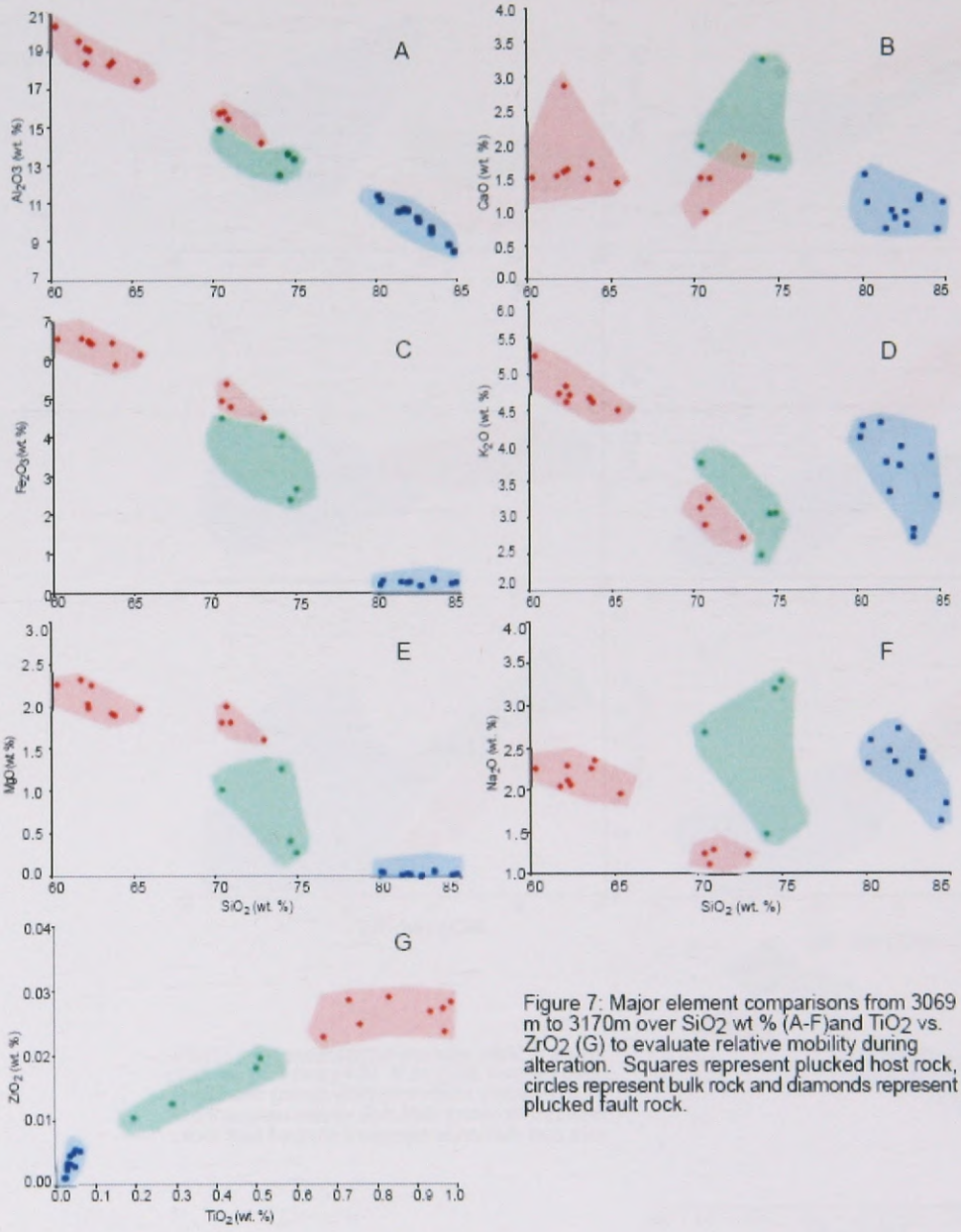

Figure 7: Major element comparisons from 3069 m to 3170m over SiO_2 wt % (A-F)and TiO_2 vs. ZrO_2 (G) to evaluate relative mobility during alteration. Squares represent plucked host rock, circles represent bulk rock and diamonds represent plucked fault rock.

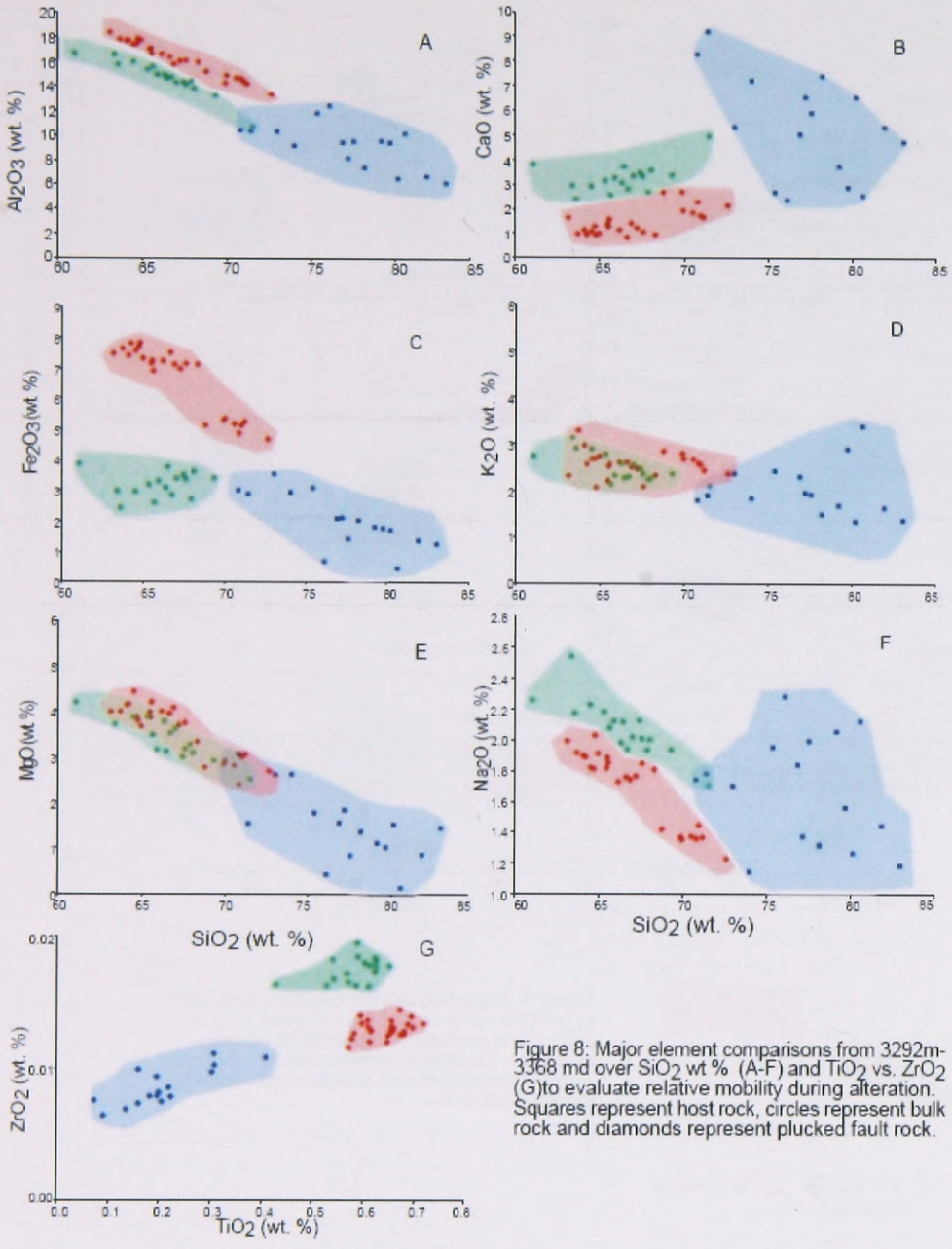

Figure 8: Major element comparisons from 3292m-3368 md over SiO_2 wt % (A-F) and TiO_2 vs. ZrO_2 (G)to evaluate relative mobility during alteration. Squares represent host rock, circles represent bulk rock and diamonds represent plucked fault rock.

Tables 1 and 2 are included in an Excel document and are presented in the next two pages.

Table 1 Average Compositions and Calculated Mass Transport	3069- 3158 m			3161- 3170 m			3292-3316 m			3319-3368 m		
	Plucked Fault Rock	Bulk Rock	Calculated mass transport (g/100 g)	Plucked Fault Rock	Bulk Rock	Calculated mass transport (g/100 g)	Plucked Fault Rock	Bulk Rock	Calculated mass transport (g/100 g)	Plucked Fault Rock	Bulk Rock	Calculated mass transport (g/100 g)
Al_2O_3	18.86 (0.90)	13.96 (1.06)	-6.04	15.31 (0.75)	12.52 (0.71)	-1.65	14.55 (0.55)	9.68 (0.14)	-0.66	17.15 (0.79)	13.43 (0.86)	0.80
BaO	0.05 (0.00)	0.25 (0.14)	-0.23	0.04 (0.00)	0.15 (0.03)	-0.11	0.04 (0.01)	0.09 (0.00)	-0.07	0.04 (0.00)	0.08 (0.02)	-0.05
CaO	1.73 (0.45)	1.85 (0.13)	-1.13	1.46 (0.32)	3.24 (0.23)	-2.20	2.19 (0.41)	4.42 (0.03)	-3.07	1.23 (0.23)	2.83 (0.36)	-1.81
Fe_2O_3	6.3 (0.25)	3.21 (1.01)	-0.55	4.91 (0.35)	4.05 (0.40)	-0.56	4.82 (0.23)	4.20 (0.33)	-1.21	6.87 (0.37)	5.17 (0.49)	0.52
K_2O	4.79 (0.26)	3.31 (0.46)	-1.30	3.02 (0.25)	2.50 (0.28)	-0.36	2.51 (0.15)	1.89 (0.19)	-0.34	2.47 (0.24)	2.27 (0.26)	-0.21
MgO	2.09 (0.17)	0.58 (0.35)	0.30	1.81 (0.15)	1.27 (0.11)	0.01	2.84 (0.20)	2.26 (0.07)	-0.50	3.97 (0.25)	3.21 (0.55)	0.09
MnO	0.14 (0.02)	0.05 (0.02)	0.01	0.04 (0.01)	0.05 (0.00)	-0.03	0.04 (0.01)	0.07 (0.00)	-0.05	0.06 (0.02)	0.07 (0.00)	-0.02
Na_2O	2.17 (0.14)	3.07 (0.38)	-2.16	1.23 (0.08)	1.49 (0.18)	-0.61	1.37 (0.06)	1.46 (0.00)	-0.61	1.86 (0.08)	1.80 (0.13)	-0.26
P_2O_5	0.13 (0.02)	0.02 (0.04)	0.03	0.23 (0.03)	0.17 (0.02)	0.00	0.46 (0.05)	0.24 (0.02)	0.02	0.18 (0.08)	0.17 (0.04)	-0.02
Rb_2O	0.02 (0.00)	0.01 (0.00)	-0.01	0.01 (0.00)	0.01 (0.00)	0.00	0.01 (0.00)	0.01 (0.00)	0.00	0.01 (0.00)	0.01 (0.00)	0.00
SiO_2	62.68 (1.55)	73.33 (2.73)	-47.01	71.17 (1.20)	74.03 (2.00)	-23.50	70.55 (1.12)	75.27 (0.16)	-31.53	65.44 (1.46)	70.49 (1.81)	-16.17
TiO_2	1.00 (0.05)	0.33 (0.14)	0.09	0.74 (0.06)	0.51 (0.07)	0.02	0.59 (0.02)	0.33 (0.04)	0.04	0.66 (0.03)	0.46 (0.03)	0.09
ZrO_2	0.03 (0.00)	0.014 (0.00)	0.00	0.03 (0.00)	0.02 (0.00)	0.00	0.01 (0.00)	0.01 (0.00)	0.00	0.01 (0.00)	0.01 (0.00)	0.00
Sum	100.00	100.00	**-58.00**	100.00	100.00	**-29.00**	99.99	99.97	**-38.00**	99.96	99.99	**-17.00**
N	8	3		4	1		8	1		17	16	

Table 2: Calculated mass change %

Oxide	3069- 3158 m	3161- 3170 m	3292-3316 m	3319-3368 m
	% change			
Al_2O_3	-43.3	-13.2	-6.8	6.0
BaO	-91.7	-78.7	-79.6	-65.7
CaO	-60.9	-68.1	-69.3	-63.9
Fe_2O_3	-17.2	-13.8	-28.9	10.1
K_2O	-39.2	-14.3	-17.8	-9.4
MgO	51.7	1.0	-22.1	2.7
MnO	12.7	-51.7	-64.6	-24.0
Na_2O	-70.3	-41.3	-41.4	-11.8
P_2O_5	122.1	-1.8	7.6	-10.1
Rb_2O	-40.4	-22.2	-8.3	8.3
SiO_2	-64.1	-31.7	-41.9	-22.9
TiO_2	28.6	3.7	11.1	19.9
ZrO_2	-16.8	-4.4	-22.4	-2.7

Appendix A: Procedures

The drill cuttings from SAFOD are stored at the United States Geologic Survey (USGS) in Menlo Park, California. Using a mechanical splitter, representative samples at 3 m intervals for depths from 3066 m to 3158 m and 3151 m to 3170 m were collected. These samples had been washed in tap water at the drill site and then air dried before being transported to the repository at the USGS.

Using a microscope, it was possible to identify fault grains within each sample. Fault rock characteristics include polished grains, slickensides and groves. These fault grains were plucked and saved for analysis. For each depth, except for 3066m where there was not enough fault material, and 3146 and 3149m where there was a contamination issue, approximately 0.1- 0.2 grams of material was plucked. In some of the samples, especially in the shallower part of each fault, this was almost all of the fault material in the sample. Closer to the fault trace the amount of fault material increased in the samples.

Because some of the fault grains appeared to have surficial iron spots, each sample was rinsed in a few milliliters of deionized water using an ultrasonic bath for approximately 1 minute. The water was decanted and the samples air dried. The dried samples were re-examined under the microscope to ensure that the iron spots had been removed and that all the material plucked was appropriate. Some of the plucked samples were photographed using a digital camera attached to a microscope. Host rocks, mainly quartz and feldspar, were also plucked and analyzed from most of the samples the same rinsing, drying and re-examining procedure was followed for those.

X-ray Diffraction

The plucked rock samples were powdered using an agate mortal and pestle. This powdered material was used to make powdered, air- oriented and glycolated X-ray diffraction (XRD) measurements for select samples. A Scintag X ray Diffractometer with CuKα radiation was used. The powdered samples were analyzed for approximately 1 hour from 2-50°2θ with a step size of 0.02 and 1 second steps. Some of the material used for the powder diffraction was re-used to make the air oriented slides. Approximately 0.05 g of powder was mixed with 1 mL of deionized water in an ultrasonic bath for ~ 1 minute. This slurry was pipetted onto a glass slide and was left to air- dry overnight. The air dried slides were prepared to allow for the orientation of the clays in the sample. These samples were analyzed for approximately 1 hour from 2-12°2θ with a step size of 0.02 with 6 second steps. Some samples were analyzed from 2-35°2θ to characterize the mineralogy. A two hour run was also performed for a few samples, but there were no major differences in the results. In order to detect the presence of swelling clays such as smectite, the air oriented slides were placed in a glycolater overnight. The glycolated samples were run with the same method as the air oriented slides. It was especially important to do a 1 hour run for the glycolated samples because the glycol evaporates- and a 2 hour run may have been too long.

MacDiff, a computer program, was used to identify the peaks seen in each spectrum. Moore and Reynolds, (1989) was also used as a reference to identify peaks.

Inductively Coupled Plasma- Optical Emission Spectrometry

To prepare the samples for Inductively Coupled Plasma- Optical Emission Spectrometry (ICP-OES) analysis, 0.1 g of sample was needed. Approximately 1 g of $LiBO_2$ and 0.1 g LiBr were combined with the sample in a platinum-gold crucible. The fluxer machine allowed for three samples per run. After heating and spinning the crucibles and their contents for approximately 5 minutes, the machine (M4 Fluxer) poured the contents into heat proof beakers containing 50 mL of 5% Trace Metal Nitric Acid and a magnetic stir bar. Each solution was mixed (by the magnetic stir bars) for approximately 5 minutes. Whenever samples were digested, USGS standards were digested also. The USGS standards were used to correct for any problems with the digestion technique. It was discovered that a consistent amount of potassium was being lost during the digestion procedure- most likely due to the presence of LiBr. This issue was controlled by analyzing standards with every sample digestion session.

The crucibles were rinsed in 10% Nitric Acid for approximately 10 minutes. The solutions were poured into pre-weighed 60 mL plastic bottles and then the bottles were re-weighed. To prepare the samples for ICP-OES analysis, 1 mL of sample was diluted with 9 mL 2% Trace Metal Nitric Acid in a disposable plastic test tube.

The ICP-OES used was a Perkin- Elmer Optima 3300DV. Before calibrating the machine, it was aligned with 5% Mn fluid. Using a certified calibration standard, SM-225102, diluted 6 times (1/10, 1/50, 1/100, 1/500, 1/1000, and 1/5000) with 8 or 9 mL 2% Trace Metal Nitric Acid + 1 mL matrix (LiBO2 + LiBr) and a blank - 1 mL of the matrix + 9 mL 2% Trace Metal Nitric Acid the machine was calibrated. The correlation coefficient for each element was ≥ 0.999. Several quality control check standards, chosen

based on their concentrations of elements of interest, were analyzed throughout the analysis to determine instrument drift.

The raw data output from the ICP-OES was converted from diluted sample to actual sample concentrations in parts per million (ppm) and then converted into weight percent oxides by dividing by the atomic weight and the molar ratio of the oxide, multiplying by the molecular weight and then dividing by 10. These data were corrected by using the USGS standards, RGM-1, QLO, BHVO, SDC and SCO, to calculate the error. The corrected samples often still over calculated silica so the concentration of silica was calculated by subtracting all of the other measured and corrected elements from 100 and the results were used for the silica concentration. This also allowed all of the sums to equal 100 %. The weight percent oxides were used in the calculations for mass balance and are shown on Figures 5,7, 8, and Appendix B.

Scanning Electron Microscopy

Polished thin sections from failed core at 3066 m and 3436 m measured depth were coated with carbon for Scanning Electron Microscopy (SEM) analysis. Electron Dispersive Spectroscopy (EDS) elemental peaks were used to identify minerals in the sections. Several back-scatter photographs were taken during this process. The SEM used was a Hitachi- S-3200N at the University of Michigan.

Appendix B is included in Excel document and is presented in the next three pages.

Appendix B: Elemental Plucked Fault Rock Data from ICP-OES

	Al2O3	BaO	CaO	Fe2O3	K2O	MgO	MnO	Na2O	P2O5	Rb2O	SiO2	TiO2	ZrO2
	[wt%ox]	[wt%ox]	[wt%ox]	[wt%ox]	[wt%ox]	[wt%ox]	[wt%ox]	[wt%ox]	[wt%ox]	[wt%ox]	[wt%ox]	[wt%ox]	[wt%ox]
10070 F	20.37	0.05	1.52	6.51	5.37	2.27	0.14	2.26	0.12	0.02	60.28	1.07	0.03
10080 F	19.59	0.05	1.54	6.50	4.82	2.33	0.16	2.05	0.12	0.02	61.73	1.06	0.03
10090 F	19.10	0.05	1.64	6.44	4.75	2.27	0.16	2.06	0.11	0.02	62.38	1.00	0.02
10100 F	19.19	0.05	1.61	6.44	4.89	2.04	0.13	2.29	0.12	0.02	62.16	1.03	0.03
10310 F	18.40	0.05	2.86	6.36	4.68	1.99	0.15	2.12	0.16	0.02	62.19	0.98	0.03
10340 F	18.31	0.05	1.50	6.39	4.70	1.93	0.13	2.26	0.14	0.02	63.59	0.96	0.02
10350 F	18.48	0.05	1.72	5.84	4.60	1.91	0.13	2.36	0.12	0.02	63.79	0.96	0.03
10360 F	17.49	0.05	1.43	6.09	4.47	1.98	0.11	1.96	0.15	0.02	65.30	0.93	0.03
10370 F	15.46	0.04	1.50	4.75	3.24	1.82	0.05	1.30	0.20	0.01	70.85	0.75	0.02
10380 F	15.76	0.04	1.51	5.07	3.20	1.81	0.03	1.26	0.23	0.01	70.32	0.73	0.03
10390 F	14.20	0.05	1.82	4.49	2.73	1.61	0.04	1.24	0.23	0.01	72.88	0.66	0.02
10400 F	15.83	0.04	0.99	5.34	2.89	2.00	0.03	1.13	0.28	0.01	70.61	0.83	0.03
10800 F	14.44	0.04	2.35	4.87	2.57	2.39	0.04	1.36	0.42	0.01	72.62	0.30	0.01
10810 F	14.46	0.04	2.64	5.02	2.66	2.69	0.04	1.39	0.51	0.01	71.80	0.30	0.01
10830 F	14.69	0.04	1.85	5.14	2.60	3.03	0.04	1.54	0.38	0.01	72.14	0.30	0.01
10840 F	14.54	0.04	1.96	5.14	2.60	2.87	0.04	1.35	0.49	0.01	72.34	0.31	0.01
10850 F	13.39	0.06	2.24	4.53	2.31	2.68	0.04	1.29	0.51	0.01	74.25	0.29	0.01
10860 F	14.47	0.04	1.91	5.08	2.65	2.82	0.04	1.38	0.43	0.01	72.48	0.30	0.01
10870 F	14.08	0.04	1.72	5.15	2.45	3.04	0.04	1.39	0.38	0.01	73.11	0.29	0.01
10880 F	14.48	0.04	2.87	5.24	2.77	2.89	0.06	1.47	0.49	0.01	71.09	0.29	0.01
10890 F	18.22	0.05	1.42	7.87	2.80	3.97	0.07	1.97	0.14	0.01	65.24	0.35	0.01
10910 F	16.73	0.05	1.08	7.05	2.48	4.26	0.06	1.83	0.22	0.01	68.02	0.36	0.01
10920 F	16.49	0.04	0.91	7.34	2.40	3.92	0.06	1.84	0.08	0.01	68.57	0.33	0.01
10930 F	17.15	0.05	0.97	7.59	2.47	4.00	0.06	1.90	0.15	0.01	67.36	0.34	0.01
10940 F	17.42	0.04	1.16	7.34	2.85	4.11	0.06	1.92	0.20	0.01	66.68	0.34	0.01
10950 F	16.76	0.04	1.19	7.10	2.61	3.94	0.06	1.80	0.18	0.01	68.02	0.32	0.01
10960 F	16.37	0.05	1.61	6.67	2.51	4.14	0.06	1.88	0.22	0.01	68.28	0.33	0.01
10970 F	15.66	0.05	1.45	6.82	2.43	4.01	0.15	1.81	0.14	0.01	69.20	0.31	0.01
10980 F	17.30	0.05	1.02	7.20	2.63	3.60	0.06	1.93	0.13	0.01	67.61	0.33	0.01
10990 F	16.74	0.05	1.30	7.02	2.49	3.80	0.06	1.90	0.15	0.01	68.11	0.33	0.01
11000 F	16.48	0.04	1.31	6.99	2.50	3.73	0.05	1.90	0.20	0.01	68.47	0.34	0.01
11010 F	16.37	0.05	1.38	6.85	2.18	3.88	0.05	1.79	0.39	0.01	68.81	0.33	0.01
11020 F	17.03	0.05	1.57	7.13	2.28	3.79	0.05	1.89	0.22	0.01	67.52	0.35	0.01
11030 F	16.03	0.04	1.10	6.81	2.09	3.70	0.06	1.92	0.14	0.01	69.68	0.32	0.01
11040 F	16.12	0.04	1.00	6.80	2.30	3.34	0.05	1.92	0.09	0.01	69.75	0.31	0.01
11050 F	17.95	0.05	1.00	7.47	2.13	3.83	0.06	2.03	0.08	0.01	64.71	0.68	0.01

Appendix B: Elemental Bulk Rock Data from ICP-OES

	Al_2O_3	BaO	CaO	Fe_2O_3	K_2O	MgO	MnO	Na_2O	P_2O_5	Rb_2O	SiO_2	TiO_2	ZrO_2
	[wt%ox]	[wt%ox]	[wt%ox]	[wt%ox]	[wt%ox]	[wt%ox]	[wt%ox]	[wt%ox]	[wt%ox]	[wt%ox]	[wt%ox]	[wt%ox]	[wt%ox]
10100 B	14.90	0.08	1.97	4.51	3.77	1.03	0.08	2.70	0.05	0.02	70.36	0.50	0.02
10200 B	13.64	0.40	1.81	2.41	3.07	0.42	0.04	3.21	0.04	0.01	74.66	0.29	0.01
10300 B	13.36	0.28	1.78	2.69	3.08	0.28	0.03	3.31	---	0.01	74.98	0.19	0.01
10400 B	12.52	0.15	3.24	4.05	2.50	1.27	0.05	1.49	0.17	0.01	74.03	0.51	0.02
10800 B	9.53	0.13	4.40	4.58	1.68	2.34	0.08	1.45	0.24	0.01	75.19	0.38	0.01
10900 B	14.93	0.10	3.41	6.39	2.46	3.76	0.08	1.90	0.21	0.01	66.22	0.51	0.01
10910 B	14.15	0.15	2.17	5.15	2.61	4.85	0.07	1.89	0.14	0.01	68.32	0.48	0.01
10920 B	14.88	0.08	2.64	5.17	2.81	3.33	0.07	2.20	0.13	0.01	68.16	0.48	0.01
10930 B	14.34	0.13	2.63	5.12	2.59	3.47	0.07	1.90	0.14	0.01	69.14	0.46	0.01
10940 B	13.79	0.11	2.83	4.88	2.50	3.47	0.06	1.88	0.14	0.01	69.85	0.46	0.01
10950 B	12.83	0.10	3.00	4.73	2.29	3.25	0.06	1.75	0.21	0.01	71.32	0.44	0.01
10960 B	13.40	0.09	2.75	4.85	2.32	3.39	0.06	1.70	0.21	0.01	70.74	0.47	0.01
10970 B	12.86	0.12	3.11	4.67	2.23	2.70	0.06	1.87	0.24	0.01	71.70	0.44	0.01
10980 B	12.40	0.12	3.20	4.83	2.04	2.77	0.07	1.67	0.19	0.01	72.27	0.42	0.01
10990 B	11.92	0.10	3.02	4.53	2.12	2.62	0.06	1.66	0.18	0.01	73.35	0.41	0.01
11000 B	12.71	0.17	2.98	5.00	2.12	2.85	0.06	1.65	0.17	0.01	71.85	0.42	0.01
11010 B	13.22	0.12	2.53	5.45	2.07	3.16	0.07	1.63	0.13	0.01	71.13	0.49	0.01
11020 B	12.93	0.08	2.41	5.14	2.02	2.94	0.06	1.66	0.12	0.01	72.15	0.48	0.01
11030 B	13.16	0.08	3.33	5.25	2.05	2.80	0.07	1.74	0.16	0.01	70.90	0.45	0.01
11040 B	13.41	0.13	2.93	5.66	2.10	2.83	0.07	1.78	0.15	0.01	70.45	0.47	0.01
11050 B	13.98	0.10	2.31	5.96	1.92	3.13	0.07	1.67	0.11	0.01	70.24	0.48	0.01

Appendix B: Elemental Plucked Host Rock Data from ICP-OES

	Al_2O_3	BaO	CaO	Fe_2O_3	K_2O	MgO	MnO	Na_2O	P_2O_5	Rb_2O	SiO_2	TiO_2	ZrO_2
	[wt%ox]	[wt%ox]	[wt%ox]	[wt%ox]	[wt%ox]	[wt%ox]	[wt%ox]	[wt%ox]	[wt%ox]	[wt%ox]	[wt%ox]	[wt%ox]	[wt%ox]
10090 H	11.40	0.12	1.56	0.22	4.12	0.06	0.01	2.32	0.02	0.01	80.09	0.06	0.01
10100 H	9.72	0.10	1.18	0.37	2.74	0.07	0.00	2.39	0.02	0.01	83.35	0.05	0.01
10300 H	10.62	0.09	0.91	0.29	3.37	0.02	---	2.74	0.02	0.01	81.90	0.03	0.00
10310 H	10.06	0.11	0.81	0.19	3.99	0.01	0.00	2.19	---	0.01	82.60	0.02	0.00
10340 H	8.85	0.15	0.74	0.24	3.84	0.02	0.00	1.65	0.02	0.01	84.45	0.02	0.00
10350 H	10.58	0.12	0.75	0.29	4.32	0.02	0.00	2.47	0.02	0.01	81.36	0.05	0.00
10360 H	10.68	0.12	1.02	0.27	3.78	0.03	0.00	2.34	0.01	0.01	81.71	0.03	0.00
10370 H	11.17	0.13	1.14	0.32	4.27	0.05	0.01	2.60	0.02	0.01	80.24	0.04	0.00
10380 H	9.47	0.17	1.23	0.32	2.85	0.05	0.01	2.46	0.00	0.01	83.37	0.04	0.01
10390 H	8.48	0.10	1.14	0.27	3.32	0.03	0.01	1.85	0.01	0.01	84.75	0.03	0.00
10800 H	9.70	0.05	3.80	1.85	1.75	1.14	0.05	2.19	0.12	0.01	79.15	0.19	0.01
10810 H	9.55	0.09	5.10	2.13	2.55	1.58	0.05	1.77	0.11	0.01	76.83	0.22	0.01
10830 H	7.52	0.05	7.46	2.07	1.60	1.38	0.08	1.37	0.13	0.01	78.14	0.20	0.01
10840 H	6.28	0.17	4.80	1.29	1.45	1.48	0.04	1.24	0.10	0.01	82.99	0.13	0.01
10850 H	10.54	0.05	8.35	3.06	2.29	3.09	0.06	1.48	0.12	0.01	70.74	0.20	0.01
10860 H	6.82	0.06	5.40	1.41	1.70	0.89	0.06	1.53	0.09	0.01	81.86	0.16	0.01
10870 H	9.30	0.06	7.27	2.98	1.88	2.63	0.10	1.20	0.29	0.01	73.96	0.30	0.01
10880 H	6.65	0.11	6.61	1.75	1.41	1.54	0.07	1.37	0.15	0.01	80.13	0.18	0.01
10890 H	10.44	0.10	5.39	3.58	2.32	2.64	0.06	1.90	0.18	0.01	72.95	0.41	0.01
10900 H	8.27	0.06	6.60	2.16	1.95	1.86	0.08	1.50	0.12	0.01	77.15	0.22	0.01
10910 H	12.54	0.17	2.43	0.73	4.89	0.45	0.02	2.57	0.03	0.02	76.06	0.09	0.01
10920 H	10.28	0.12	2.61	0.51	3.26	0.16	0.03	2.35	0.02	0.01	80.57	0.07	0.01
10970 H	9.65	0.07	5.98	1.46	1.94	0.87	0.09	2.17	0.09	0.01	77.50	0.16	0.01
10980 H	9.56	0.08	2.95	1.82	2.89	1.05	0.04	1.68	0.05	0.01	79.67	0.20	0.01
11000 H	11.94	0.06	2.76	3.13	2.41	1.80	0.04	2.09	0.11	0.01	75.34	0.31	0.01
11030 H	10.47	0.05	9.25	2.93	1.91	1.56	0.11	1.96	0.08	0.01	71.35	0.31	0.01

Appendix C: Other Work

The age of exhumation friction melts along the Alpine Fault New Zealand- in press, Geology, 2007 by Laurence Warr, Ben van der Pluijm and Sara Tourscher

The age of exhumed friction melts along the Alpine Fault, New Zealand

L.N. Warr[a], B.A. van der Pluijm[b] and S. Tourscher[b]

[a]Centre de Géochimie de la Surface (CNRS-ULP), 1 rue Blessig, 67084-Strasbourg, France

[b]Department of Geological Sciences, University of Michigan, Ann Arbor, MI 48109, U.S.A.

Abstract

Laser ablation $^{40}Ar/^{39}Ar$ step heating analysis of 20 pseudotachylyte veins from a single location along the exhumed central portion of the active Alpine Fault of New Zealand yield total gas age values between 1–19 Ma. Evidence is presented that these veins are genetically related and formed during coeval episodes of seismogenic melting at upper crustal depth, conflicting with a spread in formation ages. Rather, the total gas ages show an exponential decrease with increasing proportion of melt matrix and K content. The young values (<1.2 Ma) correspond to high K_2O (>3%), matrix-rich samples and the older (>8 Ma) correspond to low K_2O (<1%), matrix-poor lithologies. These relationships indicate that incomplete degassing and mixtures of radiogenic argon sources characterize these samples, controlled by the degree of melting related to lithological differences and fractionation between clasts and matrix components. The true age of melt generation can be extrapolated from the flat portion of the exponential curve, indicating a young episode of crystallization and cooling between 0.9 and 1.2 Ma.

Assuming an average exhumation rate up to 9 mm/year for this period of uplift and erosion, these results imply that these friction melts were generated 8-11 km depth, during a major Quaternary slip episode along a relatively anhydrous segment of the Alpine Fault, lying between the infiltration of downward meteoric and upflowing metamorphic crustal fluids. In contrast to previous interpretations, the introduction of excess argon into the host rocks occurred

prior to the generation of these melts and is not related to the friction process. We conclude that reliable dating of friction melt events can be made by pre-selecting reservoir veins high in potassic and matrix content.

Keywords: $^{40}Ar/^{39}Ar$ dating, pseudotachylyte, coseismic faults, friction melt, upper crust, Alpine Fault

INTRODUCTION

Pseudotachylytes, the product of friction melting during large magnitude earthquakes, provide a unique opportunity to study the mechanism and age of coseismic faulting in the geological record (Sibson, 1975; Di Vincenzo et al., 2004; Di Toro et al., 2006). These clast-ridden melts have been described in a broad range of lithospheric depths originating during faulting of the mantle (Austrheim and Boundy, 1994), the crust (Magloughlin, 1992) and land slides at the surface (Masch et al., 1985). Despite the diverse occurrence, it remains a key challenge to isotopically date these melts, which is required to catalogue in time and space large paleoseismic events in the geological record. In cases where the rate of fault exhumation is constrained, accurate age determinations of pseudotachylytes can also provide depth estimates for crustal melting.

The principle method used for dating the cooling age of friction melt events in crustal fault zones is the $^{40}Ar/^{39}Ar$ isotopic technique, determined by step-heating or laser ablation methods (Merrihue and Turner, 1966; Magloughlin et al., 2001; Sherlock and Hetzel, 2001; Mueller et al., 2002; Di Vincenzo et al., 2004). Determining the true age of a frictional heating event requires i) all inherited radiogenic argon is outgassed from the melt, ii) no inherited argon

components are present in unmelted clasts, and iii) no externally derived excess argon gas accumulates in the sample following crystallization. In the case of natural pseudotachylytes, these conditions are commonly not fulfilled due to the incomplete and heterogeneous nature of flash melting and the trapping of argon-bearing fluid inclusions in clasts (Di Vincenzo et al., 2004).

The complexities of argon degassing during friction melting are mirrored both by the relative rarity of simple degassing curves that show well defined plateau ages and by the significant variations in total gas age measured on pseudotachylyte veins (Kohut and Sherlock, 2003). Despite these problems, significant, age determinations have been obtained by laser probe dating of melted matrix portions of pseudotachylyte veins and assessment of mixed argon sources as indicated by elevated Ca/K and Cl/K ratios (Kelly et al., 1990, Sherlock and Hetzel, 2001, Mueller et al., 2002). The successful dating of young pseudotachylytes presents a particular challenge in that the amount of radiogenic argon is too low for effective laser probing of the vein matrix. Here, $^{40}Ar/^{39}Ar$ laser ablation study of small matrix-rich rock fragments appears to be the best approach (Magloughlin et al., 2001, Warr et al., 2003)

In this study we examine the nature of $^{40}Ar/^{39}Ar$ variations for 20 geologically young pseudotachylyte veins collected from a single location at the northwest end of the active, central section of the Alpine Fault, New Zealand. Besides offering an excellent example of natural friction melts, this area is of interest as previously analyzed pseudotachylytes displayed a very large range of isotopic age values in well-developed veins (Adams, 1981, Warr et al., 2003). This region of the Southern Alpines also has a well constrained exhumation, uplift and erosion history over the last 5 Ma (Batt et al., 2000). Our objective was to test whether the friction melts of seemingly differing age were generated at various crustal depths, or whether the melts are coeval

and therefore formed at a specific time and depth during the exhumation history of the fault. The latter would require an alternative explanation for the range in observed ages that is not related to variable depth melting. Based on the mineralogic, isotopic and geochemical variations presented, we demonstrate that all sampled pseudotachylytes formed during the Quaternary, within a single, upper crustal generation zone in a relatively anhydrous segment of the Alpine Fault.

GEOLOGICAL SETTING AND PSEUDOTACHYLYTE SAMPLES

The Alpine Fault represents an active, oblique slip segment of the Australian–Pacific plate boundary (Fig. 1). The central section is characterized by a steep thrust geometry with high rates of dextral strike-slip displacement (27+/-5mm/year) and rapid exhumation of Pacific hanging wall rocks at rates of up to 10 mm/year (Cooper and Norris, 1994; Norris and Cooper, 2001). Examples of pseudotachylyte veins and their structural relationships along the Alpine fault have been studied by Reed (1964), Wallace (1976), Sibson et al. (1979) and Bossière (1991).

The 20 samples of pseudotachylyte analyzed here were collected to the east of the village of Hari Hari, mainly from the Harold Creek section (Fig. 1a). The majority of samples were obtained from boulder material washed down from the fault trace. Additional samples included in this study were provided by R. Sibson (Otago University), originating from the same locality and from the nearby Wanganui River section.

The sample blocks contain a mixture of thin source veins formed along melt generation surfaces and thicker, reservoir veins. Based on 515 measurements the vein thickness ranges from 1 to 73 mm, with an average value of 7 mm (Fig. 1b). The thicknesses shows an asymmetrical distribution skewed towards thinner veins. The peak maximum is at 3 mm and has a shoulder at

7-8 mm. The source veins are typically 3 mm or less in thickness, whereas the reservoir veins vary, and locally are several centimeters across. Faults zones exposed in large boulders typically contain parallel sets of planar melt generation surfaces (Fig. 1c, d). These surfaces are concordant to the lithological layering and represent the principle planes of displacement. Transported melt was injected into fractures that are parallel or at high angles to the displacement surfaces. Some of these fracture surfaces are notably listric in shape (Fig. 1c).

The pseudotachylytes selected for isotopic study were the reservoir veins thicker than 3 mm, as they are considered to be more suitable for dating purposes due to their higher matrix content. At the sampling location, the melts were derived from mylonitized amphibolite quartzo-feldspathic schists of the garnet-oligoclase zone, which represent metamorphosed greywacke lithologies of the Alpine Schist (Grapes, 1995). The high silica content of the host rock indicates intermediate to felsic compositions (Warr and van der Pluijm, 2005).

The fault rocks of the Hari Hari section lie at the northeastern end of the highly exhumed central section of the Alpine Fault. Based on low $^{40}Ar/^{39}Ar$ hornblende ages as young as 3-5 Ma at the Franz-Josef Glacier, Little et al. (2005) estimated a maximum time-integrated exhumation rate of ~6 to 9 mm/year for this section. This is in accordance with the high late Quaternary dip slip rate of >12mm/year at Gaunt Creek (Cooper and Norris 1994), located ~30 km SW of Hari Hari and the 7 to 9 mm/year regional uplift rate determined from displaced post-glacial marine/terrestrial sediments of the Paringa River (located a further 80 km to the SW). The rate of uplift is considered to decrease to the north of the Hari Hari location. Just 20 km to the NE, Quaternary dip slip estimates range between 5-7 mm/year (Norris and Cooper 2001).

ANALYTICAL METHODS

Rock slabs oriented perpendicular to vein margins were cut from the sample blocks. Polished thin sections were prepared for optical and scanning electron microscopy (SEM) and back-scattered electron (BSE) images were obtained by traversing across the veins at a magnification of 500x. The relative abundance (%) of clast and matrix components was measured on the basis of varying grey scales and size properties using area-related parameters of the NIH Image Analysis software (http://rsb.info.nih.gov/nih-image/). The method allows effective separation of the larger quartz and feldspar clasts from very fine-grained, phyllosilicate-rich, neocrystallized matrix. The analytical procedure followed that outlined by Warr and van der Pluijm (2005) .

Powder preparations of the vein material were studied by X-ray diffraction (XRD) analysis to determine the principle mineral assemblages and by inductively coupled plasma – optical emission spectroscopy (ICP-MS) in order to determine elemental concentrations. For geochemical analyses samples were fusion digested using $LiBO_2$ and the analytical results corrected for volatile content determined from loss-on-ignition (LOI). The K concentration used in this study is expressed as $\%K_2O$ (Table 1), and the accuracy of the experimental procedure was tested against USGS standards of known elemental concentrations (standards rgm-1a, qlo-1, SDC-1 and bhvo-1).

Laser ablation $^{40}Ar/^{39}Ar$ step-heating was undertaken on mm-size (~0.01g) rock chips that were selected to minimize clast content. The analytical details are similar to that used by Lo Bello et al. (1987) and Magloughlin et al. (2001). An initial test of encapsulated verses non-capsulated samples showed consistency between total gas ages and argon-retention ages, indicating recoil effects to be negligible. The fraction of $^{39}Ar_{(K)}$, $^{38}Ar_{(Cl)}$,and $^{37}Ar_{(Ca)}$ released during step heating was used to establish ^{39}Ar, Ca/K and Cl/K degassing spectra, following

application of correction factors. Total gas ages, a description of the shape of ^{39}Ar spectra, and mean Ca/K and Cl/K values, are given in Table 1.

RESULTS

The pseudotachyte veins typically consist of a matrix composed of quartz-plagioclase-biotite with opaques and occasional chlorite (Table 1). Common opaque phases observed are magnetite and ilmenite. Minor amounts of hornblende were detected only in sample pst6-2. Clast components consist of quartz, plagioclase and some opaque minerals; only in the matrix-poor sample of pst4-1 are phyllosilicate phases observed in clast form. Based on published microprobe data, the principal K-bearing mineral phase of these samples is biotite (mean of 9 wt%K_2O) and minor amounts of orthoclase feldspar, present in clast form (mean 0.12 wt% K_2O). Only in the potassic-poor veins (pst4-1 and pst24 1) is the feldspar likely to contribute significantly to the ^{39}Ar signature, with high >5 Ca/K ratios for these samples.

The proportion of matrix and clast components present, expressed as %matrix, ranges between 48 to 89 % (Table 1). These correspond to wear/melt ratios of 0.12-1.13, whereby the wear/melt ratio = (Tmelt - Tcrust)/Tmelt (O'Hara, 2001). As a general observation, the matrix rich samples are veins containing the most biotite, which is also indicated by the good correspondence between % matrix and K_2O content. The K_2O ranges from 0.32 K_2O wt% in the sample characterized by 47% matrix (pst4-1) to 4.37 K_2O wt% for the 89% matrix-rich vein (pst9-1).

The $^{40}Ar/^{39}Ar$ total gas ages range from old values of 18.63Ma+/-0.23 for the matrix-poor, low K_2O sample (pst4-1) to young ages of 0.95Ma+/-0.23 for the matrix and K_2O-rich vein of pst9-1. The ^{39}Ar spectra show a range of degassing patterns that can be grouped into three

types: saddle, stepped and near-plateau shapes (Table 1, Fig. 2). Saddle-shaped spectra are the most common (11 of the 20 samples), and characterize the full range of total gas ages measured. The oldest age spectra show very pronounced troughs whereby very old age values correspond to the early and late stages of ^{39}Ar release (approaching 180 Ma in Fig. 2a). These peak ages correspond with elevated Cl/K ratios and indicate significant quantities of excess argon, possibly present as trapped fluid inclusions within quartz clasts (Di Vincenzo et al., 2004). Stepped profiles characterize 5 vein samples yielding younger total gas ages values (2.36 - 6.36+/-0.05 Ma). The progressive increase in the fraction of degassed ^{39}Ar with increasing temperature commonly corresponds with slight increases in the Cl/K ratio (Fig. 2b) and likely reflects mixtures of externally derived excess argon and internally sourced argon that was not degassed during the friction melting episode. Near plateau type spectra characterize 4 vein samples ranging in the age from 0.95 to 4.71 Ma+/-0.05 Ma. These patterns are defined by constant degassing of ^{39}Ar over 60 – 65 % of the release spectra, and usually correspond to plateaus in the Cl/K release spectra (Fig. 2c).

Correlation plots between the total gas ages, % matrix, K_2O content and the Ca/K and Cl/K ratios reveal systematic relationships between the measured parameters (Figure 3). An exponential decrease in total gas age occurs with increasing % matrix (R^2 = 0.94, n = 12). The cluster of points around ca. 1 Ma represents a plateau in the curve, corresponding to total gas ages of 0.95 – 1.12 +/-0.02 Ma. An exponential decrease in the total gas age is also observed with increasing K_2O content (R^2 = 0.81; n = 12). In this case, the ca. 1 Ma plateau line corresponds with veins containing > 3 wt% K_2O. An exponential increase in K_2O content also corresponds to the increasing % of matrix (Fig. 3c; R^2 = 0.90; n = 12). Linear trends are observed when plotting the total gas age against Ca/K and Cl/K ratios (R^2 = 0.91 and 0.66, respectively; n

= 20). Ca/K and Cl/K values are observed to generally increase linearly with total gas age, and show intercepts between 0 and 1 Ma.

DISCUSSION AND CONCLUSIONS

The 20 pseudotachylyte veins studied from a single location along the rapidly exhumed, central section of the Alpine Fault are characterized by large variation in total gas ages (ca. 1–19 Ma), % matrix (48-89 %) and K-content (0.32 - 4.37 wt% K_2O). The well defined exponential decrease in age with increasing % matrix and potassic content is found, which is a clear indication of mixed argon sources. The occurrence of pronounced trough shape degassing spectra and age values, well in excess of the regional background levels of the biotite cooling ages (<2 Ma; Batt et al. 2000), indicate that many of the veins contain excess argon. Similar patterns were described in the host rock mylonite schist of a pseudotachylyte from this location (Warr et al. 2003) with total gas ages of ~9.5 Ma and older. Ages approaching 180 Ma during the early and late stages of ^{39}Ar release, and the correspondence of old ages with quartz-feldspar rich lithologies (i.e., low K_2O), imply excess argon stored in the clast fraction, probably as trapped fluid inclusions within quartz (Di Vincenzo et al. 2004). That this component of inherited argon gas decreases with the increase in % melt matrix suggests the excess argon was introduced into the system prior to friction melting and not during subsequent alteration. The source of this externally derived radiogenic argon is not clear, but may be derived from the circulation of deeper seated metamorphic fluids as proposed by others (Stern et al., 2001; Wannamaker et al., 2002).

The excess argon introduced into the system prior to frictional melting, and the internally generated radiogenic argon that accumulated following cooling of the fault rocks through the

biotite and plagioclase closure temperatures (within the last 6 Ma), was only completely degassed in potassic-rich veins where the melt fraction exceeded 85%. This condition was satisfied in just 3 of the 20 melt layers measured and represents the true age of frictional melting for the material studied (0.9 to 1.2 Ma). Importantly, the well defined correlations between age values, matrix abundance and potassic content indicate they belong to the same genetic group, forming under similar conditions and crustal depths. If significantly older or younger friction melt events occurred along this segment of the Alpine Fault, we would expect that such clear correlations between the degree of melting and the isotopic age values would not exist. A minimal influence from clast components in these samples is reflected by near plateau to slightly stepped spectra with low Ca/K (<0.4) and Cl/K (0.04) ratios.

Adopting a 6 to 9 mm/year exhumation rate for last 1 Ma (Little et al 2003), the interpreted age of frictional melting can be used to constrain the depth of paleo-seismic faulting to 5 to 11 km. Reasonable estimates of the regional crustal temperatures at these depths can be obtained from the isotopic behavior and the petrology of the fault rock material. The young $^{40}Ar/^{39}Ar$ biotite total gas ages (<1.2 Ma) indicate that the crustal temperature must have been lower than the biotite closure temperature of ca. 300°C. Estimates based on the modeled isotherms of Shi et al. (1996) also imply temperatures ranging between 200 and 300°C for these depths along the fault zone. Above this level the formation of hydrous clay minerals in fault gouge implies significant infiltration of down-flowing meteoric waters. The absence of friction melts at depth >11 km may reflects the presence of deeper seated, highly pressured metamorphic fluids predicted on the basis of magnetotellic data and low seismic waves (Stern et al. 2001; Wannamaker et al. 2002). The zone of melting is therefore suggested to correspond to an

anhydrous segment of the Alpine Fault, lying somewhere between the infiltration of downward meteoric and upflowing metamorphic crustal fluids.

The friction melt temperatures of the pseudotachylytes are more difficult to define accurately and probably varied on the small scale. Temperatures >1300°C appear likely due to the general assimilation of oligoclase (melting point ~1350 °C; Deer et al., 1978). Some magnetite melt textures observed by high resolution transmission electron microscopy (pst2) indicate that even the ~1600°C limit was locally exceeded. Adopting a T_{crust} range of 200-300°C and a T_{melt} range of 1300-1600°C, a wear to melt ratio of around 0.69-0.70 (ca. 59 %matrix) is predicted based on the theoretical considerations of O'Hara (2001). The marginal melt layer of pst3-3 is the only sample that matches this value. The majority of veins are enriched in matrix suggesting significant fractionation between clasts and melt occurred during injection of these reservoir veins.

Our study shows that age and formation depth of pseudotachylytes can be reliably constrained by the relationships between ages, potassic content and matrix fraction. Varying ages do not negate the use of the Ar method, but show progression toward complete melting of host rock that can be quantified. In particular, analyzing samples with varying, high K_2O content and/or matrix percentage, constrains formation ages by correlation of the chemical and textural characteristics of pseudotachylytes. These results indicate that accurate and meaningful age values for friction melt events can be obtained by laser ablation 40Ar/39Ar step heating analysis of the potassic- and melt-rich portions of pseudotachylyte reservoir veins. Improvements in the dating of these rocks would benefit considerably by pre-selection of samples based on chemical and textural characteristics prior to time-consuming isotopic analyses.

Acknowledgements

$^{40}Ar/^{39}Ar$ isotopic analyses, electron microscopy and ICP-MS analyses were carried out at the University of Michigan. We thank U-M's Chris Hall and Ted Huston for technical support. Research was supported by grants from the US National Earthquake Hazards Reduction Program (USGS-04HQGR0066) and the US National Science Foundation (EAR-0230055 and 0345985). Rick Simpson and Simon Cox are also thanked for their helpful discussions and logistical support.

References

Adams, C.J. (1981). Uplift rates and thermal structure in the Alpine Fault Zone and alpine schists, Southern Alps, New Zealand. Geological Society of London Special Publication, 9, 211-222.

Austrheim, H. and Boundary, T.M. (1994). Pseudotachylytes generated during seismic faulting and ecologitization of the deep crust, Science, 265, 82-83.

Batt, G.E., Braun, J., Kohn, B.P. and McDougall, I. (2000). Thermochronological analysis of the dynamics of the Southern Alps, New Zealand. Geological Society Bulletin, 112, 250-266.

Bossière, G., 1991. Petrology of pseudotachylytes from the Alpine Fault of New Zealand. Tectonophysics 196, 173-193.

Cooper, A.F., Norris, R.J., 1994. Anatomy, structural evolution, and slip rate of a plate-boundary thrust: The Alpine fault at Gaunt Creek, Westland, New Zealand, Geological Society of America. Bulletin, 106, 627-633.

Di Toro, G., Hirose, T., Nielsen, S., Pennacchioni, G. and Shimamoto, T. (2006). Natural and experimental evidence of melt lubrication of faults during earthquakes. Science, 311, 647-649.

Di Vincenzo, G., Rocchi, S., Rossetti, F. and Storti, F. (2004). 40Ar-39Ar dating of pseudotachylytes: the effect of clast-hosted extraneous argon in Cenozoic fault-generated friction melts from the West Antarctic Rift System. Earth and Planetary Science Letters, 223, 349-364.

Grapes, R.H., 1995, Uplift and exhumation of Alpine schist, Southern Alps, New Zealand: Thermobarometric constraints: New Zealand Journal of Geology and Geophysics, 38, p. 525–533.

Kelly, S.P., Reddy, S.M. and Maddock, R. (1994). Laser-probe 40Ar/39Ar investigation of a pseudotachylyte and its host rock from the Outer Isles thrust, Scotland. Geology, 22, 443-446.

Kohut, M. and Sherlock, S. (2003). Laser microprobe 40Ar-39Ar analysis of pseudotachylyte and host-rocks from the Tatra Mountains, Slovakia: evidence for late Paleogene seismic/tectonic activity. Terra Nova, 15, 6, 417-424.

Little, T.A., Cox, S., Vry, J.K. and Batt, G. (2005). Variations in exhumation level and uplift along the oblique-slip Alpine fault, central Southern Alps, New Zealand. Geological Society of America Bulletin, 117, 707-723.

Lo Bello, Ph., Fraud, G., Hall, C.M., York, D., Lavina, P. & Bernat, M. 1987. 40Ar/39Ar step-heating and laser fusion dating of a Quaternary volcanic from Neschers, Massif Central, France: The defeat of xenocrystic contamination, Chemical Geology. (Isotope Geoscience), 66, 61-71.

Magloughlin, J.F., Hall, C.M. and van der Pluijm, B.A. (2001). 40Ar-39Ar geochronometry of pseudotachylytes by vacuum encapsulation: North Cascade Mountains, Washington, USA. Geology, 29, 51-54.

Magloughlin, J.F., Spray, J.G. 1992. Frictional melting processes and products in geological materials: Introduction and discussion. Tectonophysics, 204, 197-204.

Masch, L., Wenk, H.R. and Preuss, E. (1985) Electron microscopy study of hyalomylonite, Tectonophysics, 115 131-160.

Merrihue, C. and Turner, G. (1966). Potassium-argon dating by activation with fast neutrons. Journal of Geophysical Research, 71, 2852-2857.

Mueller, W., Kelly, S.P. and Villa, I.M. (2002). Dating fault-generated pseudotachylytes: comparison of 40Ar/39Ar stepwise-heating, laser-ablation and Rb-Sr microsampling analyses. Contributions to Mineralogy and Petrology, 144, 57-77.

Norris, R.J., Cooper, A.F., 2001. Late Quaternary slip rates and slip partitioning on the Alpine Fault, New Zealand. Journal of Structural. Geology., 23, 503-520.

O'Hara, K., 2001. A pseudotachylyte geothermometer. Journal of Structural Geology, 23, 1345-1357.

Reed, J.J., 1964. Mylonites, cataclasites, and associated rocks along the Alpine Fault, South Island, New Zealand. N.Z. Journal of Geology and Geophysics, 7, 654-684.

Sherlock, S.C. and Hetzel, R. (2001). A laser probe 40Ar/39Ar study of pseudotachylite from the Tambach Fault Zone, Kenya: direct isotopic dating of brittle faults. Journal of Structural Geology, 23, 33-44.

Sibson, R.H., 1975. Generation of pseudotachylyte by ancient seismic faulting. Geophysical Journal of the Royal Astronomical Society, 43, 775-794.

Sibson, R.H., 1994. Crustal stress, faulting and fluid flow. In: Geofluids, Origin, Migration and Evolution of fluids in Sedimentary Basins. Geological Society of London Special Publication, 78, 69-84.

Sibson, R.H., White, S.H., Atkinson, B.K., 1979. Fault rock distribution and structure within the Alpine Fault Zone: a preliminary account, Royal Society of New Zealand, 18, 55-65.

Stern, T., Kleffmann, S., Okaya, D., Scherwath, M., Bannister, S. (2001). Low seismic-wave speeds and enhances fluid pressures beneath the Southern Alps of New Zealand. Geology, 29, 679-682.

Wallace, R.C., 1976. Partial fusion along the Alpine Fault Zone, New Zealand. Geological Society of America Bulletin, 87, 1225-1228.

Warr, L.N., Cox, S.C., 2001. Clay mineral transformations and weakening mechanisms along the Alpine Fault, New Zealand. Geological Society of London Special Publication, 186, 85-101.

Warr, L.N., van der Pluijm, B.A., (2005). Crystal fractionation in friction melts of seismic faults (Alpine Fault, New Zealand). Tectonophysics, 403, 111-124.

Warr, L.N., van der Pluijm, B.A., Peacor, D.R., Hall, C.M. 2003. Frictional melt pulses during a ~1.1 Ma earthquake along the Alpine Fault, New Zealand. Earth and Planetary Science Letters, 209, 39-52.

Word count 4003 including references

Figures and Tables

Fig. 1. a) Map of New Zealand showing the location of pseudotachylyte veins (white point) collected at Harold Creek, along the Alpine Fault (af). hh = town of hari hari. b) Frequency of vein thickness at Harold Creek based on 522 measurements of structures exposed in stream boulders. c) Typical pseudotachylyte veins lying parallel to compositional layering of the Alpine Schist. Numerous reservoir veins are seen crossing at high-angles to the layering. d) irregular-shaped, thick reservoir veins formed adjacent to a set of fault generation surfaces.

Fig. 2. a) Three typical BSE images (magnification x 500) of the pseudotachylyte veins with 47, 69 and 88 % matrix development. The clasts are composed of either quartz (dark grey) or feldspar (medium grey).

Fig. 3. Plot showing an exponential relationship between the total gas ages verses the % matrix content as determined by image analysis. b) Plot of total gas age verses K concentration measured by ICP.

Table 1. Summary of results for the 20 pseudotachylte veins studied in detail. The character of the veins was determined by hand specimen examination and optical microscopy. The mineral assemblage was determined by combined XRD and SEM study. The % of matrix was measured by image analysis of SEM backscattered images. The wear/melt ratios (O'Hara 2001) are given in brackets. The weight % (wt%) of K_2O was determined by ICP-MS. The total gas ages, the shape of the degassing ^{39}Ar spectra, and the mean Ca/K and Cl/K ratios, were calculated from the concentrations of ^{40}Ar, ^{39}Ar, ^{38}Ar and ^{37}Ar isotopes.

	Optical	XRD – SEM		SEM	ICP-MS	Argon gas analyses			
sample	character	matrix minerals	clast minerals	matrix %	K_20 wt%	total gas age (Ma)	spectra	mean Ca/K	mean Cl/K
pst2-1	central melt layer vein	Qtz, Pl, Bt, Mag, Ch, Opq	Qtz, Pl Opq	88 (0.14)	3.18	1.08 +/- 0.01	plateau	0.40	0.004
pst2-2	marginal melt layer	Qtz, Pl, Bt, Magt, Ch, Opq	Qtz, Pl Opq	78 (0.28)	2.55	1.73 +/- 0.02	saddle	0.40	0.005
pst2-3	marginal melt layer	Qtz, Pl, Bt, Mag, Opq	Qtz, Pl, Opq	78 (0.28)	2.55	2.23 +/- 0.05	saddle	1.00	0.005
pst3-1	central melt layer	Qtz, Pl, Bt, Mag, Ch, Opq	Qtz, Pl, Opq	74 (0.21)	1.34	4.71 +/- 0.05	plateau	2.04	0.007
pst3-2	marginal melt layer	Qtz, Pl, Bt, Mag, Ch, ,	Qtz, Pl, Opq	48 (1.08)	0.82	12.61 +/- 0.14	saddle	3.30	0.008
pst3-3	marginal melt layer	Qtz, Pl, Bt, ,Mag, Ch,	Qtz, Pl, Opq	58 (0.72)	0.83	8.73 +/- 0.15	saddle	2.88	0.009
pst3-6	adjacent vein	Qtz, Pl, Bt, Mag	Qtz, Pl, Opq	Nd	1.21	3.55 +/- 0.08	saddle	1.65	0.007
pst4-1	homogenous vein	Qtz, Pl; Mag, Ch, Bt	Qtz, Pl, Opq, Bt, Ch	47 (1.13)	0.32	18.63 +/- 0.23	saddle	7.28	0.025
pst6-2	homogenous vein	Qtz, Pl, Mag, Bt, Hbl, Ch	Nd	Nd	1.68	6.36 +/- 0.05	stepped	2.07	0.007
pst7-2	layered vein	Qtz, Pl, Mag, Bt, Ch	Nd	Nd	1.73	4.72 +/- 0.012	saddle	1.03	0.005
pst9-1	homogenous vein	Qtz, Pl, Bt, Mag,	Qtz, Pl, Opq	89 (0.12)	4.37	1.12 +/- 0.01	stepped	0.16	0.004
pst10-2	homogenous vein	Qtz, Pl, Bt, Mag, Ch	Qtz, Pl, Opq	80 (0.25)	2.21	2.36 +/- 0.03	stepped	0.84	0.004
pst10-3	homogenous vein	Qtz, Pl, Bt, Mag, Ch	Qtz, Pl, Opq	80 (0.25)	2.29	2.95 +/- 0.04	stepped	0.82	0.005
pst10-4	homogenous vein	Qtz, Pl, Bt, Mag, Ch	Qtz, Pl, Opq	Nd	2.32	2.29 +/- 0.03	plateau	0.97	0.004
pst13-1	layered vein	n.d	Qtz, Pl, Opq,	69 (0.51)	1.82	4.25 +/- 0.05	stepped	1.85	0.006
pst13-2	layered vein	Qtz, Pl, Bt, Mag, Ch	Qtz, Pl, Opq,	Nd	1.35	5.59 +/- 0.05	saddle	2.22	0.006
pst13-3	layered vein	Qtz, Pl, Bt, Mag, Ch	Qtz, Pl, Opq,	Nd	2.24	5.29 +/- 0.06	saddle	1.62	0.006
pst13-4	layered vein	Qtz, Pl, Bt, Mag, Ch	Qtz, Pl, Opq,	Nd	1.84	7.90 +/- 0.13	saddle	2.63	0.012
pst14-1	homogenous vein	Qtz, Pl, Bt, Ch	Qtz, Opq	88 (0.18)	3.40	0.95 +/- 0.02	plateau	0.37	0.004
pst24-1	homogenous vein	nd	Nd	nd	0.34	10.53 +/- 0.32	saddle	5.14	0.004

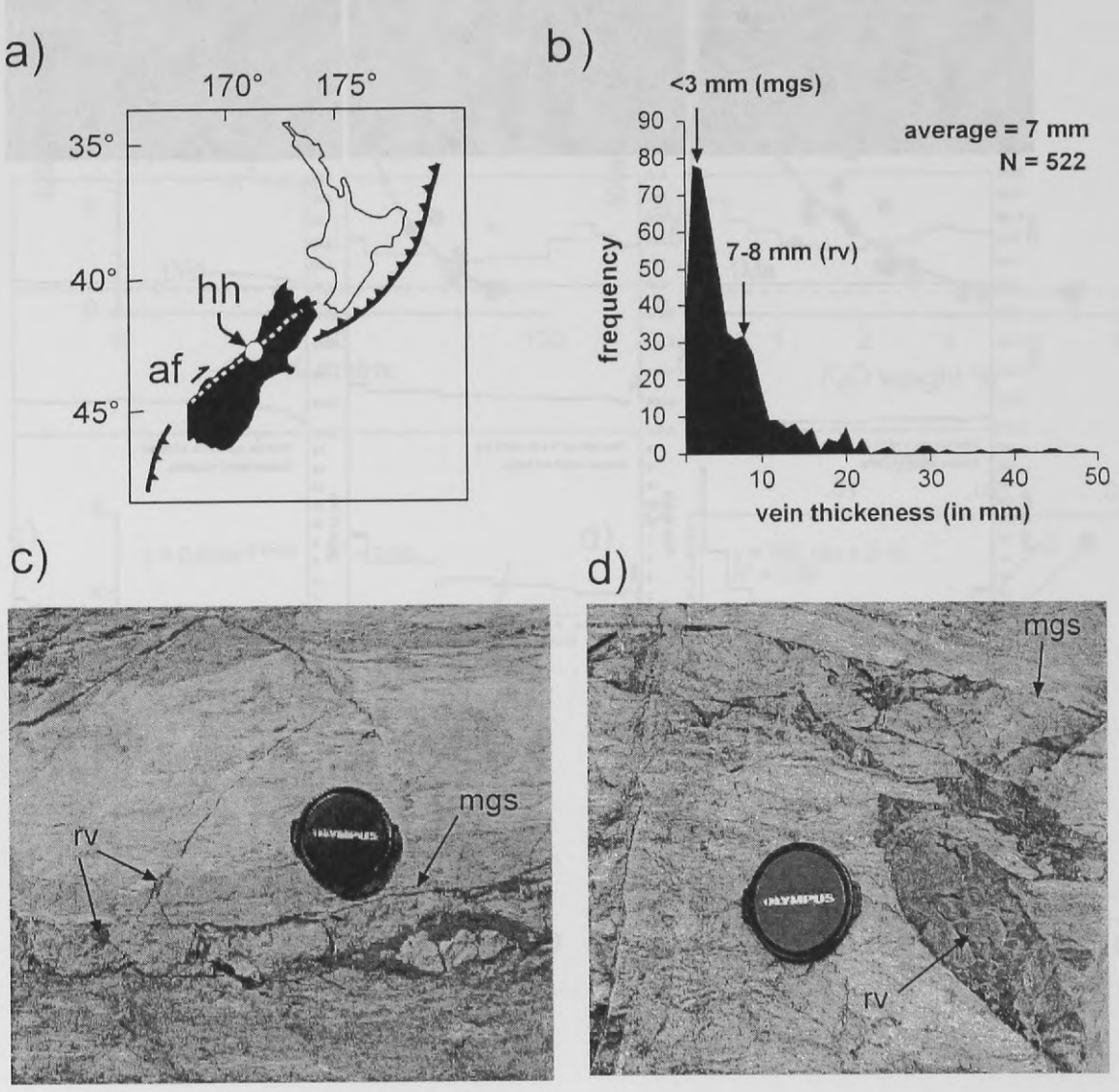
a)
170°
175°
35°
40°
45°
hh
af
b)
<3 mm (mgs)
average = 7 mm
N = 522
7-8 mm (rv)
frequency
90
80
70
60
50
40
30
20
10
0
10
20
30
40
50
vein thickeness (in mm)
c)
rv
mgs
d)
mgs
rv

Fig. 1

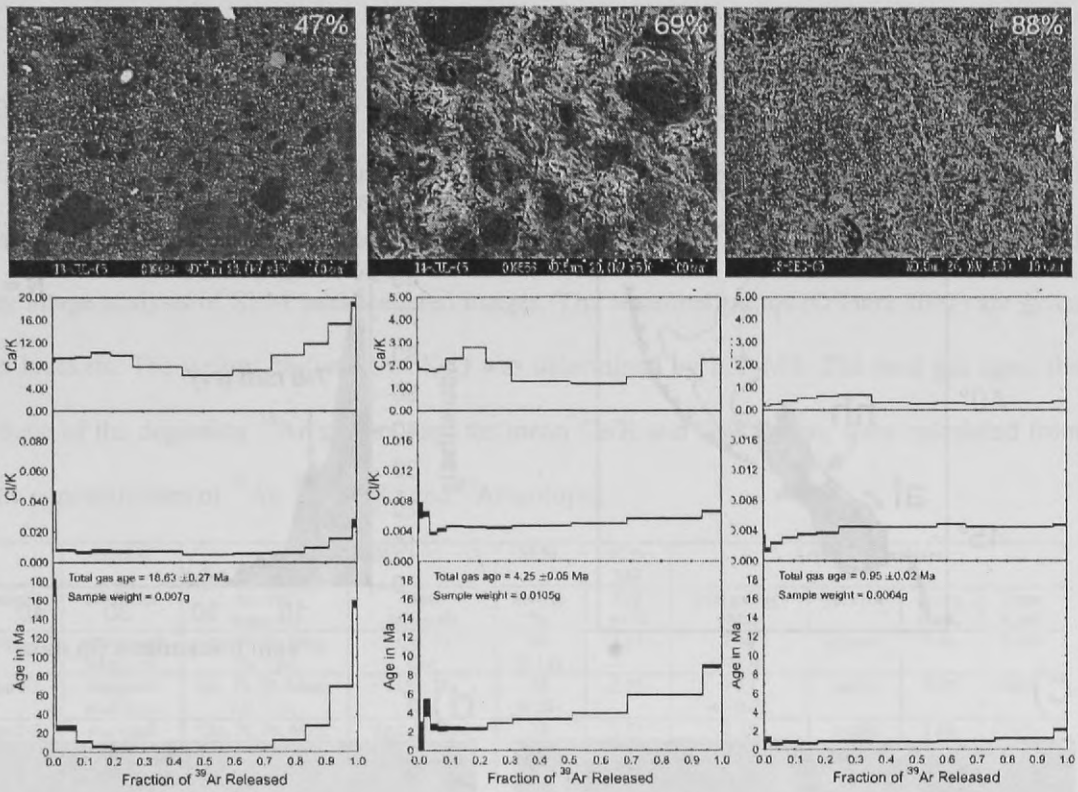
47%
69%
88%
Ca/K
Cl/K
Age in Ma
Total gas age = 16.63 ±0.27 Ma
Sample weight = 0.007g
Total gas age = 4.25 ±0.05 Ma
Sample weight = 0.0105g
Total gas age = 0.95 ±0.02 Ma
Sample weight = 0.0064g
Fraction of ^{39}Ar Released

Fig. 2

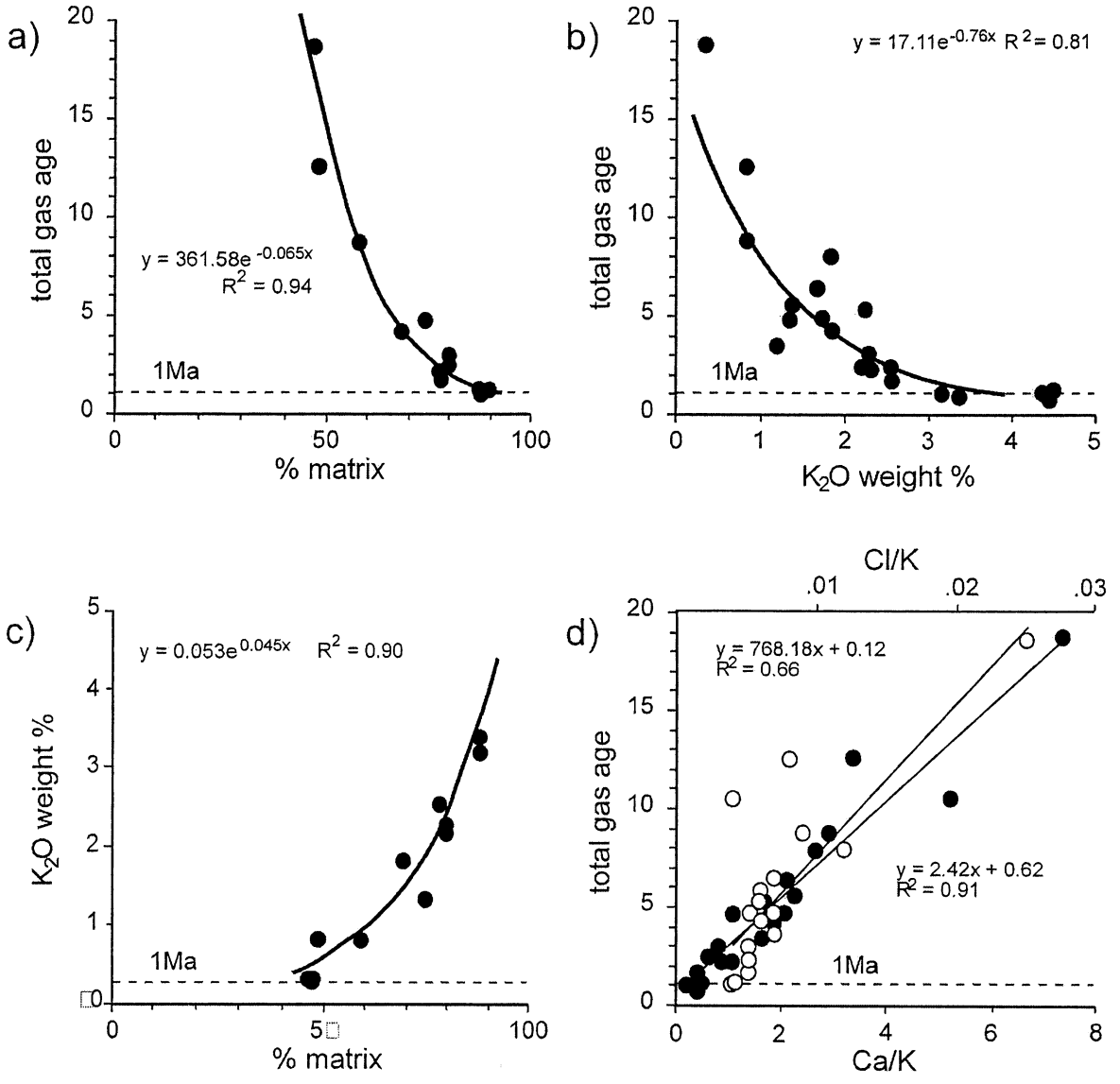
a)
total gas age
% matrix
y = 361.58e -0.065x
R2 = 0.94
1Ma
b)
y = 17.11e-0.76x R2 = 0.81
total gas age
K2O weight %
1Ma
c)
K2O weight %
% matrix
y = 0.053e0.045x R2 = 0.90
1Ma
d)
Cl/K
total gas age
Ca/K
y = 768.18x + 0.12
R2 = 0.66
y = 2.42x + 0.62
R2 = 0.91
1Ma

Fig. 3